RESEARCH ARTICLE

Characterizing trade-wind shallow convection regimes in the open sea with a synergy of ship-based vertical profiling observations

Claudia Acquistapace[1] | Sabrina Schnitt[1] | Sibylle Krause[1] | Nils Risse[1] | Diego Lange[2] | Dwaipayan Chatterjee[1,3]

[1]Institute for Geophysics and Meteorology, University of Cologne, Cologne, Germany

[2]Institute of Physics and Meteorology, University of Hohenheim, Stuttgart, Germany

[3]Karlsruhe Institute of Technology (KIT), Karslruhe, Germany

Correspondence
Claudia Acquistapace, Institute for Geophysics and Meteorology, University of Cologne, Pohligstrasse 3, 50969 Cologne, Germany.
Email: cacquist@uni-koeln.de

Abstract

Precipitation occurs frequently in observed shallow convection across the Northern Atlantic Trades. Despite its central role in shaping the water cycle, it remains challenging to quantify how much and when precipitation occurs, and how precipitation shapes its immediate thermodynamic and dynamic environment. Here we make use of the synergy of active profiling remote sensing aboard the *RV Maria S. Merian* during the Elucidating the Role of Clouds–Circulation Coupling in Climate (EUREC^{4}A) field study in 2020. We investigate the thermodynamic and dynamic conditions before, during, and after precipitation using a statistical approach. By distinguishing between shallow and congestus profiles according to observed cloud geometrical thickness, we find that congestus clouds occur more frequently than shallow (21% and 9% of profiles), contain three times more liquid water (60 vs. 22 $g \cdot m^{-2}$), and precipitate more often (71% vs. 7%). Shallow clouds, as a precursor stage to congestus, show little variability during the day, while congestus clouds maximize at night. Convection is initiated in shallow clouds located in patches of humidity $1\, g \cdot kg^{-1}$ moister than the clear-sky state, sometimes coupled with sea-surface induced changes in the sub-cloud layer. At the congestus stage, microphysical and thermodynamic processes trigger further cloud and precipitation growth in the cloud layer. In shallow conditions, virga induce a cooling and moistening anomaly in the sub-cloud layer that fosters cold-pool development. In precipitating congestus clouds, dry, cold air is found in sub-cloud and cloud layers. By analyzing a case study with multiple datasets, we recorded a variation in the vertical velocity field at cloud top associated with the development of precipitation and connected with a change in mesoscale cloud patterns. The statistics presented, as well as the case study, can serve as a benchmark dataset for studying the precipitation life cycle in high-resolution modeling.

KEYWORDS

cloud organization, cold pools, deep learning, EUREC^{4}A, marine boundary layer, precipitation, shallow convection, ship-based profiling remote sensing

1 | INTRODUCTION

Shallow cumulus clouds forming in the trade-wind region are crucial in understanding how the climate will respond to Earth's radiative forcing (Bony & Dufresne, 2005; Vial *et al.*, 2013). They exert a net radiative cooling effect on the Earth's radiation budget (Bony *et al.*, 2004). This cooling, occurring locally at the cloud scale, induces shallow circulation patterns (Naumann *et al.*, 2017), that, in given conditions, can produce organized cloud structures at the mesoscale. Such cloud organizations, in turn, modulate the cloud radiative response (Bony *et al.*, 2020) in a crucial coupling for climate feedback that embraces multiple scales. Also, precipitation shapes these spatial organization patterns repeatedly, as various studies based on satellite observations and field campaigns show (Nuijens *et al.*, 2009; Snodgrass *et al.*, 2009). The way these complex multi-scale cloud processes are represented in climate models causes a substantial inter-model spread (Nujens & Siebesma, 2019) in cloud feedback as a response to climate sensitivity (Bony & Dufresne, 2005; Vial *et al.*, 2013).

Precipitation is common in the trades and accounts for around 20%–30% of the total precipitation in tropical regions (Lau & Wu, 2003; Radtke *et al.*, 2022; Short & Nakamura, 2000). In the last decades, various campaigns in the trades investigated convection processes and demonstrated the essential role of moisture transport for convection and the hydrological cycle (Holland & Rasmusson, 1973; Siebesma *et al.*, 2003; Stevens *et al.*, 2001). More recently, the Rain in Cumulus over the Ocean (RICO) campaign (Rauber *et al.*, 2007) showed that rain rates larger than $1 \, \text{mm} \cdot \text{h}^{-1}$ are frequent in the region. Nuijens *et al.* (2009) showed further that precipitation is almost always present and detailed the relationship between precipitation amounts, boundary-layer conditions, and cloud properties. Zuidema *et al.* (2011) studied the impact of cold pools on the subsequent organization of convection, showing that larger rain rates are often associated with cloud clusters organized in arc shapes. Cold pools were detected during the Dynamics of the Madden–Julian Oscillation (DYNAMO) experiment (Yoneyama *et al.*, 2013) using the temperature drop at the surface. Using this same methodology, Vogel *et al.* (2021) compiled a 10-year climatology of cold pools from the Barbados Cloud Observatory record. They found that cold pools occur on at least 73% of the analyzed days and are associated with a mean rain rate of $0.9 \, \text{mm} \cdot \text{h}^{-1}$. Moreover, 50% of the cold pools are associated with clouds with a maximum cloud-top height greater than 3 km.

Given that cloud aggregation is often necessary for and associated with precipitation, what are the processes and environmental conditions leading to this aggregation? Modeling studies showed that sea-surface temperature

(SST: Li & Carbone, 2012), surface fluxes, and radiative feedback might contribute to cloud organization (Bretherton *et al.*, 2005). Large eddy simulations (LES) have helped to explain how precipitation influences the formation of cloud patterns. Precipitation can force the transition from closed to open cells via fostering decoupling and cloud organization via cold pools (Wang & Feingold, 2009). Seifert and Heus (2013) showed that precipitation evaporating on the local cloud scale was essential for triggering cluster aggregation. More recently, Vogel *et al.* (2016) argued that precipitation modulates the vertical dynamics and thermodynamics of clouds in the trades, determining their structure. Bretherton and Blossey (2017) developed cumulus convection in a large-domain LES model by exploiting the cumulus cloud field's instabilities with respect to humidity anomalies. By creating perturbations in the cloud layer, the instabilities due to the humidity anomalies amplify moist and dry patches and develop advective aggregation by encouraging mesoscale circulations. Finally, an interesting and innovative Lagrangian LES approach was presented by Narenpitak *et al.* (2021) to describe the transition of shallow clouds to organized clustered cloud structures. They also showed that precipitation is not needed for aggregation, and that large-scale vertical velocity regulates the transition to the aggregated state by modulating the turbulent kinetic energy production in the cloud layer as the cloud deepens. In summary, LES studies show a variety of possible mechanisms linked to cloud aggregation and precipitation. However, the complexity of modeling different dimensional scales and processes still represents one limitation of the studies above.

The Elucidating the Role of Clouds–Circulation Coupling in Climate (EUREC^{4}A) field campaign took a novel, multiscale observing approach to investigate interactions across different scales (Bony *et al.*, 2017; Stevens *et al.*, 2021). EUREC^{4}A occurred east of Barbados in January–February 2020 and conducted simultaneous observations of macrophysical cloud properties and their large-scale environments. A diverse set of platforms was used, with a wealth of fine-scale observations to characterize cloud properties and their mesoscale organization, designed to help address open questions on what controls organization, shallow cloud layer depth, and convective mass flux. George *et al.* (2023) used EUREC^{4}A radiosonde observations and satellite data to identify the presence of shallow mesoscale overturning circulations (SMOCS) ubiquitous in the lowest 2–3 km, demonstrating that convergence is associated with sub-cloud and cloud layers approximately $0.7 \, \text{g} \cdot \text{kg}^{-1}$ moister than the divergent sub-cloud areas. Moreover, Radtke *et al.* (2022) used polarimetric Doppler radar (Poldirad) observations to show that precipitation cell sizes range from 2.8–20 km,

and precipitation does not occur randomly but due to inhomogeneities in the field. They found that clustering maximizes when, in dry regimes, cells are sparse, thus playing an essential role in maintaining precipitation amounts in dry conditions. New advances in cold-pool research came from modeling and observations. Rochetin *et al.* (2021) developed a conceptual model that describes the density currents that induce cold pools: the cold air spreading at the surface enhances turbulence and generates a mixed layer of limited depth where potential temperature is constant. This framework is the basis for Touzé-Peiffer *et al.* (2022)'s method using EUREC⁴A radiosondes to characterize cold pools across platforms. They found that cold pools were 1 K colder and $1\,g \cdot kg^{-1}$ moister than the environment and identified "moisture rings" as regions of positive specific humidity anomalies of $1–2\,g \cdot kg^{-1}$ near the edges of the cold pools.

Recent efforts have been made to classify cloud mesoscale patterns in the trades, utilizing human and unsupervised machine-learning methods to distinguish types (Janssens *et al.*, 2021). Various studies also focused on detecting and classifying cloud mesoscale patterns and exploited artificial intelligence (AI) to distinguish them (Chatterjee *et al.*, 2023, 2024; Denby, 2020, 2023; Rasp *et al.*, 2020; Stevens *et al.*, 2020). Radtke *et al.* (2022) investigated the organization of rain cells with moisture regimes using polarimetric C-band radar, but could not provide information on the evolution that clouds undergo in their early formation stages before reaching the precipitating stage. Many other studies linked the spatial organization of the human-labeled cloud patterns identified in satellite images to precipitation (Schulz *et al.*, 2021; Vial *et al.*, 2021). However, it is challenging to detail the processes occurring in the sub-cloud layer from a satellite due to sensor limitation and thus a lack of relevant information on the processes driving the changes in the cloud organization they observe. Moreover, the human-labeled patterns do not represent the entire cloud organization variability of the trade-wind region (Schulz *et al.*, 2021). At the same time, radiosonde data are single profiles that typically drift from the point they are launched, and it would be beneficial, as Touzé-Peiffer *et al.* (2022) also suggest, to add continuous profiling of the sub-cloud layer dynamics and thermodynamics to monitor the impact of cold pools precisely.

This work's unique set of active remote-sensing profilers can provide a holistic description of the convection and precipitation regimes existing in the trade-wind region. We aim to characterize how shallow convection depends on and impacts the surrounding environment using a unique set of ship-based profiling instruments operating on the research vessel *Maria S. Merian* (*RV*

MSM), the track of which spanned a region in the ocean east and south of Barbados during the EUREC⁴A campaign (Figure 1a). Characterizing the complete dynamics and thermodynamics of the cloud and precipitation evolution is possible using the synergy of remote-sensing profilers on board. Millimeter wavelength radar detects the presence of precipitation in the vertical profile, while Doppler lidars (DLs) measure profiles of vertical and horizontal wind speeds. In addition, the Atmospheric Raman Temperature and Humidity Sounder (ARTHUS) Raman lidar (Lange *et al.*, 2019) measures temperature and humidity profiles, as well as profiles of sensible and latent heat fluxes, characterizing the evolution of the marine boundary layer fully and filling the gaps of satellite observations.

In this study, exploiting this setup, we aim to address the following questions regarding how clouds form and evolve in the trade-wind region and how precipitation develops and impacts the marine boundary layer.

- How do shallow and congestus clouds evolve when the amount of liquid water in the cloud increases? When does this evolution mainly take place during the day, and in which dynamic and thermodynamic conditions does it occur?
- When shallow and congestus clouds form, how do the dynamic and thermodynamic fields deviate from the mean observed diurnal cycle?
- How often does it rain in the trades? How frequently does virga occur compared with precipitation reaching the ground, and how do they impact the marine boundary layer?

Our work is organized as follows. In Section 2, we describe the ship-based measurements and datasets used in the article. In Section 3, we classify the ship-based profiles in shallow and congestus clouds and introduce the method for classifying satellite images based on deep learning we used in the analysis. In Section 4, we analyze cloud macroscopic properties, as well as their daily cycle. Then, in Section 5, we investigate dynamical and thermodynamical processes initiating clouds and precipitation, and study their impact on the boundary layer during and after precipitation and virga events. In Section 6, we look in detail at a case study of a system of congestus clouds, highlighting the observed changes at the local scale through ship-based observations, as well as at the mesoscale by looking at the geostationary satellite and reanalysis datasets from ERA5 (Hersbach *et al.*, 2020). We conclude the article in Section 7 and give an outlook on future work expanding from the analyses presented here.
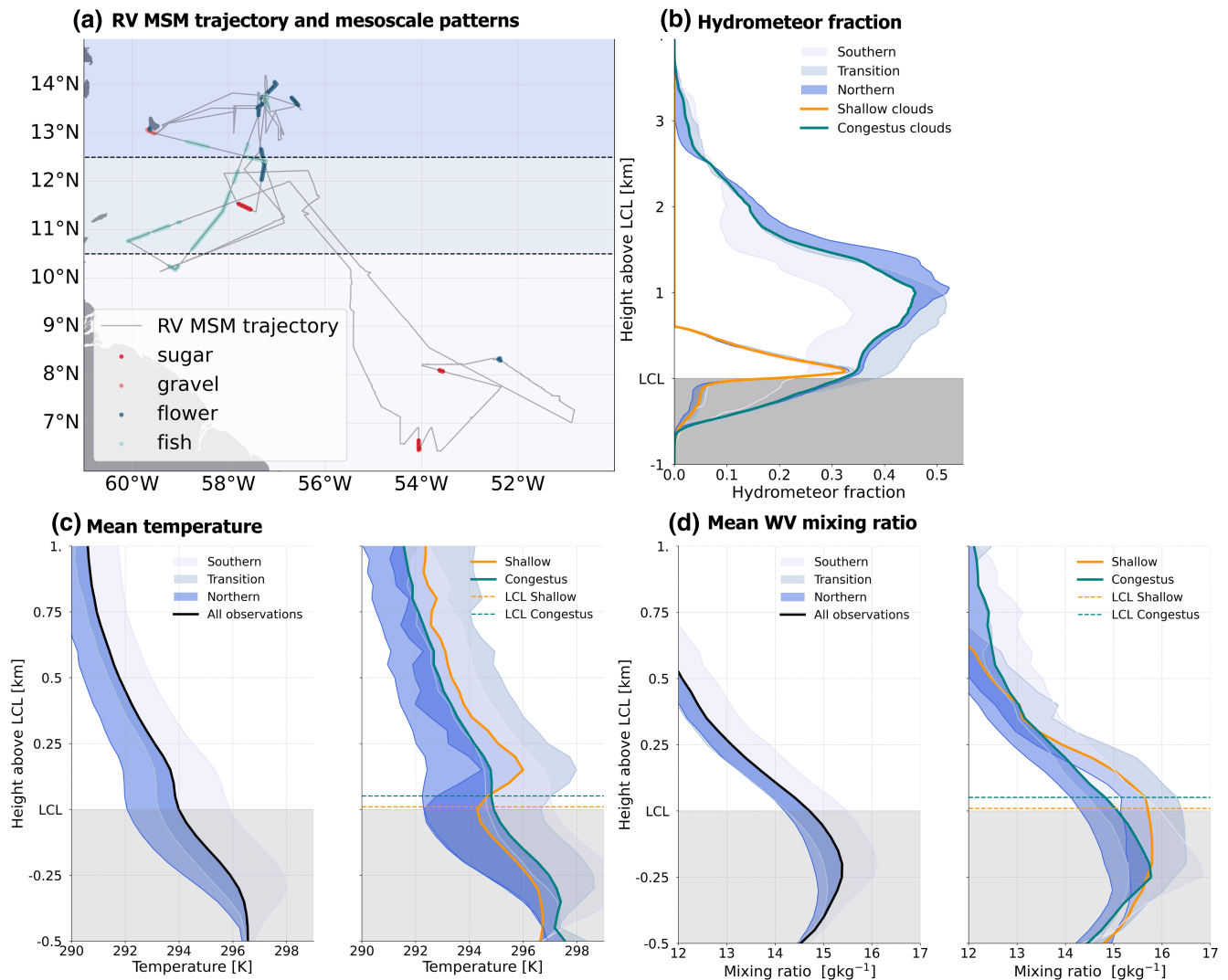
FIGURE 1 Variability of clouds and environmental conditions with latitude. (a) The trajectory of the *RV MSM* during the campaign. Overplotted on the ship track are the locations where cloud scenes were classified from satellite as flower (blue), fish (light blue), sugar (red), and gravel (pink) according to the human-label classification from Schulz (2022). (b) Variability of hydrometeor cloud fraction for shallow (orange) and congestus (green) with latitude for Northern (> 12°N, dark blue), Transition (> 9°N and < 12°N, light blue), and Southern (4 < 9°N, lavender) domains. The colored areas in (b) indicate the variations with respect to the shallow/congestus profile obtained from the whole campaign. (c) and (d) Same as in (b) but for mean temperature and mixing-ratio profiles, without distinction for shallow and congestus cloud types. Mean profiles over the entire domain are reported in black. [Colour figure can be viewed at wileyonlinelibrary.com]

2 | OBSERVATIONS ABOARD THE *RV MARIA S. MERIAN*

This work makes use of multiple ship-based profiling observation datasets collected on board the *RV MSM* and the co-located satellite observations from the Advanced Baseline Imager (ABI) on board the *Geostationary Operational Environmental Satellites* (*GOES-R*: Schmit *et al.*, 2005). Between January 19, 2020, and February 19, 2020, the *RV MSM* spanned an area extending from 6°N–13.8°N and 51°W–60°W (see Figure 1a). In this section, we provide details on the data used. For calculating meteorological quantities from the datasets presented

in this section, we used the many available routines in the open-source Metpy libraries.[1] The lifting condensation level is calculated from the ship observations using the Metpy routine based on the algorithm from Romps (2017), while profiles of equivalent and virtual potential temperatures for radiosoundings, ARTHUS Raman lidar data, and also ERA5 data are obtained with Metpy standard scripts.

2.1 | Cloud radar

A frequency-modulated continuous-wave (FMCW) 94-GHz dual-polarization radar equipped with an 89-GHz

radiometric channel observed cloud and precipitation profiles continuously with 3-s time resolution and three vertical chirps with resolutions 7.5, 9.2, and 34.1 m, and corresponding range intervals of 100–1233, 1233–3000, and 3000–10,000 m, respectively. We installed the instrument on a stabilization platform from the US Atmospheric Radiation Measurement (ARM) program Mobile Facility 2 (AMF2) to correct the Doppler radar observations for ship motions. Acquistapace *et al.* (2022a) provide details on the radar instrument, stabilization platform, and algorithm applied to correct the FMCW radar observations for ship motions. In this work, we also use liquid water path (LWP) observations with a time resolution of 3 s retrieved from the 89-GHz channel as described in Schnitt *et al.* (2024). We derived cloud radar Doppler spectra and Doppler spectra moments, and calculated diurnal cycles of cloud macroscopic properties.

2.2 | Raman and Doppler lidar

ARTHUS (Lange *et al.*, 2019) operated continuously on *RV MSM* from January 24, 2020 to February 19, 2024 to detail temperature (T) and water-vapor mixing ratio (WVMR) profiles in the sub-cloud layer with a temporal resolution of 10 s and a vertical resolution of 7.5 m. It emits 355-nm radiation pulses into the atmosphere at 200 Hz with a pulse energy of ~100 mJ, and collects the backscattered radiation in channels sensitive to elastic scattering, water vapor, and rotational Raman scattering. The receiving telescope is a Ritchey–Chrétien–Cassegrain type. Its primary mirror has a diameter of 40 cm. Raman lidars struggle to observe through clouds, due primarily to strong signal attenuation (tiny water droplets scatter and absorb laser light strongly). Therefore, ARTHUS is capable of observing through thin clouds and light rain, but not through optically thick clouds or heavy rain. ARTHUS measurements are valid from 250 m upwards, due to the geometrical overlap that affects lidars.

In addition to ARTHUS, two DLs from Streamline XR from HALO Photonics (Pearson *et al.*, 2009) installed on *RV MSM* measured the wind field. One of them operated in zenith stare mode to retrieve vertical velocity next to ARTHUS, while the second one operated in a six-beam velocity azimuth display (VAD) to retrieve horizontal wind speeds. The scanning pattern was configured in step and stare mode, with five beams pointing at azimuth angles of 0°, 72°, 144°, 216°, and 288°, with a 45° elevation angle, while the sixth beam pointed vertically. Both DLs had, in vertical staring mode, a vertical resolution of 30 m and an integration time of 1 s. In VAD mode, the vertical resolution is 20 m with an integration time of 90 s. The nominal maximum range is 12 km, but the effective maximum range depends on the amount of aerosol scatterers and clouds in the atmosphere.

For the sensible and latent heat-flux calculation, temperature, water-vapor mixing ratio, and vertical wind were averaged over one hour, every 10 min. Therefore, the final resolution is 10 min and 50 m. An averaging time of one hour is typically long enough to include enough large turbulent eddies to reduce the flux sampling errors to acceptable levels (Behrendt *et al.*, 2020; Späth *et al.*, 2022; Wulfmeyer *et al.*, 2016).

We apply some post-processing to reduce the amount of noise in the data. All variables are averaged over 10-s integration time to reduce the impact of ship motions. Moreover, we removed all values outside a given range of reasonable values, that is, from 0 to 30 g · kg^{-1} for WVMR, from 280 to 330 K for T, from −5 to 5 m · s^{-1} for vertical wind velocity (W), and from 0 to 20 m · s^{-1} for horizontal wind velocity (v_H). Moreover, we calculated the diurnal cycle of WVMR, T and vertical and horizontal wind. We then calculated anomalies relative to the daily mean values that might be due to specific atmospheric conditions like cold pools. The vertical profiles of the variables are averaged every 15 min at the same time of day. The result is a profile representative, for each time stamp, of the diurnal variability in the region. The daily cycle is interpolated back to the original time resolution and subtracted from the original time series to obtain anomalies relative to the most representative state. Since we make synergistic use of the observations from Doppler and Raman lidars and FMCW radar, we compare the size of the volumes scanned by each instrument. Table 1 shows the horizontal volume resolved by the instruments at 1000 m, a typical height where clouds are located in the trades. The FMCW radar has a horizontal resolution at 1000 m of 19.5 m. ARTHUS also has a quite broad horizontal resolution at 1000 m of 100 m, while DLs observe three orders of magnitude smaller horizontal resolutions.

2.3 | Radiosoundings

We made use of radiosounding data for investigating the environmental conditions in the presence of virga and rain and for providing an independent evaluation of the lidar observations. For these purposes, we exploited the Level 2 vertically gridded dataset produced by Stephan *et al.* (2021), a valuable dataset of 118 ascent and 38 descent soundings for the *RV MSM*. For evaluating the impact of precipitation on the lidar observations, we compared temperature profiles obtained from radiosoundings with the lidar profiles in precipitating and non-precipitating conditions. We found that, in the sub-cloud layer, the bias between radiosonde and ARTHUS temperature values is

TABLE 1   Comparison of sampling characteristics for the different instruments on board the *RV Maria S. Merian*: wavelength λ, beam width σ in degrees, vertical resolution Δh in meters, horizontal resolution at 1000 m H_{res}^{1000}, and temporal resolution Δt in seconds.

	FMCW	DL (vertical)	DL (VAD)	ARTHUS
λ [mm]	3.2	1.5×10^{-3}	1.5×10^{-3}	3.5×10^{-4}
σ	0.56	7×10^{-4}	7×10^{-4}	2.86
Δh [m]	7.5, 9.2, and 34.1[a]	30	20	50
H_{res}^{2000} [m]	19.5	0.025	0.025	100
Δt [s]	3	10[b]	90	10

[a] 7.5 between 100 and 1233 m, 9.2 between 1233 and 3000 m, 34.1 between 3000 and 10,000 m.

[b] After post-processing; original time resolution is 1 s.

within 2 K. The comparison is given in Figure S1 in the Supporting Information.

2.4 | Reanalysis data

We used reanalysis data from ERA5 (Hersbach *et al.*, 2020) to investigate the conditions of the tropospheric subsidence and air humidity for a case study we selected to characterize the evolution of a system of congestus precipitating clouds presented in Section 6. We extracted fields of temperature, specific humidity, pressure, altitude, and wind components for an area defined by latitudes between 6° and 15° and longitudes between −51° and −61°.

3 | CLOUD CLASSIFICATION

In this section, we present the cloud classification methods we use in our analysis. The cloud profiles observed from the ship are always part of cloud structures that often span large areas. On one hand, we are interested in classifying the vertical cloud profile to understand better the stage of development of the cloud we observed. In Section 3.1, we introduce the classification we adopt to distinguish shallow and congestus cloud profiles. At the same time, capturing the mesoscale classification of cloud patterns is interesting, to understand what vertical structure is observed in the presence of a given spatial cloud pattern, as seen from satellite. This analysis is presented in Section 3.2.

3.1 | Classification for vertical cloud profiles: shallow and congestus classification

For our cloud-profile classification, we follow the approach of Nuijens *et al.* (2009) and Jacob *et al.* (2020),

who sample clouds in two groups based on their geometric properties. Also, Vial *et al.* (2023) recently investigated the transitions between deeper night-time cumuli and shallower ones during the day. Analogously, here we define "shallow clouds" as all clouds with cloud tops ranging within 600 m from the lifting condensation level (LCL) height. All clouds with a cloud top between 600 and 4000 m above the LCL are instead classified as "congestus clouds".

The threshold approach is based on the observed and forward-simulated lidar and radar signals displayed in fig. 5 of Jacob *et al.* (2020). In this work, we do not exclude rainy periods as done in Vial *et al.* (2019). Therefore, our cloud classes instead reflect their two classes with cloud tops higher or smaller than 1.3 km. In our data, the LCL ranges between 600 and 700 m, and thus LCL+600 m is approximately 1.3 km, which corresponds to the height Vial *et al.* (2019) used for discrimination. Our two classes also agree with the peaks of the bimodal distribution of cloud tops found by Albright *et al.* (2023).

Finally, we sorted precipitating profiles into two different categories based on their FMCW radar reflectivity profiles. A profile is rainy if it has some radar reflectivity values below the cloud base. Cloud base was detected by applying an optimally identified threshold on the vertical gradient of the backscatter ratio from ARTHUS Raman lidar zenith-pointing observations. This method is a standard procedure in the literature (Pal *et al.*, 1992). A profile is defined as rainy at the surface if it is a rainy profile and also displays radar reflectivity values larger than −55 dBZ below 300 m. Almost all precipitation occurs in congestus clouds, which account for 71% of the time stamps classified as precipitation, while shallow precipitation only occurs 7% of the time.

The peculiar ship track followed by the *RV MSM* allows the investigation of the hydrometeor fraction profiles and environmental condition variability with latitude (Figure 1). Shallow cloud profiles show almost no variability with latitude, occurring 33%, 30%, and 37%

of the time in the Southern (<9°N), Transition (>9°N and <12°N), and Northern (>12°N) domains, respectively. Only below the lifting condensation level, which is a proxy for cloud-base height, do we notice slight differences in the hydrometeor fraction profiles caused by virga: the Southern domain shows more virga below the cloud base compared with the Northern region. Congestus profiles instead show a more substantial variability with latitude, occurring 27%, 28%, and 45% of the times in Southern, Transition, and Northern domains, respectively. The Southern region shows a reduction in hydrometeor fraction of up to 0.1 within 2 km from the LCL. Concerning precipitation, most of the congestus precipitation sampled in the campaign occurs in the Northern region (47%), while 32% is found in the Transition region and only 20% in the Southern domain. In comparison, we notice a 0.05–0.1 increase in hydrometeor fraction from cloud base up to 2 km from the LCL in the Transition and Northern regions. Also, the height at which we observe the maximum peak of the hydrometeor fraction is slightly below 1 km from the LCL in the Southern regions. It stands, instead, above 1 km from the LCL in the Transition and Northern areas. The variability around the temperature and mixing-ratio mean profile over the entire domain is illustrated in the leftmost panels of Figure 1c,d: while northern regions are approximately 1 K colder and 0.5–1 g · kg^{-1} drier than the mean profiles, in the southern regions temperatures can be up to 1.5 K and 0.5 g · kg^{-1} warmer and moister. The transition region is more similar to the southern regions, with smaller (halved) negative anomalies relative to the mean state compared with the northern region. Interestingly, the temperature and water-vapor mixing-ratio profiles change

shape for shallow versus congestus clouds (see the rightmost panels of Figure 1c,d). The profiles in congestus conditions are similar in shape to the ones observed during the entire campaign, but on average 2–4 K warmer than the general mean. The shallow profiles show a clear increase in temperature right above the LCL, possibly due to latent heat release caused by condensation and cloud formation. In terms of water-vapor mixing ratio, we do not see strong differences from the general mean profile, except for slightly higher mixing-ratio values at 500 m in the sub-cloud layer and at 250 m above the LCL. For shallow conditions, instead, the profile of water-vapor mixing ratio stays constant from 500 m up to the LCL, indicating more efficient sub-cloud layer mixing. Moreover, values at the LCL are approximately 1 g · kg^{-1} larger than in congestus conditions, suggesting moister conditions that facilitate cloud formation. Overall, given the limited values of anomalies compared with the variability observed in the diurnal cycle (see section 4.2) and the similarity in the shapes of the profiles across the different regimes, we decided to calculate the variability across the entire region without subdividing it into latitude-based regions.

Even though our data span a broad range of cloud bases and cloud tops (Figure 2a), clouds occur mainly in two different modes. The shallow mode includes profiles with cloud tops on average within 300 m from cloud base (see Table 2, where we characterized congestus and shallow clouds in terms of liquid water path, rain rate, cloud base, and cloud-top distributions). The congestus mode includes clouds with cloud tops occurring more than 1000 m from the cloud base and LWP three times larger than in the shallow cases. In precipitating congestus profiles, cloud tops
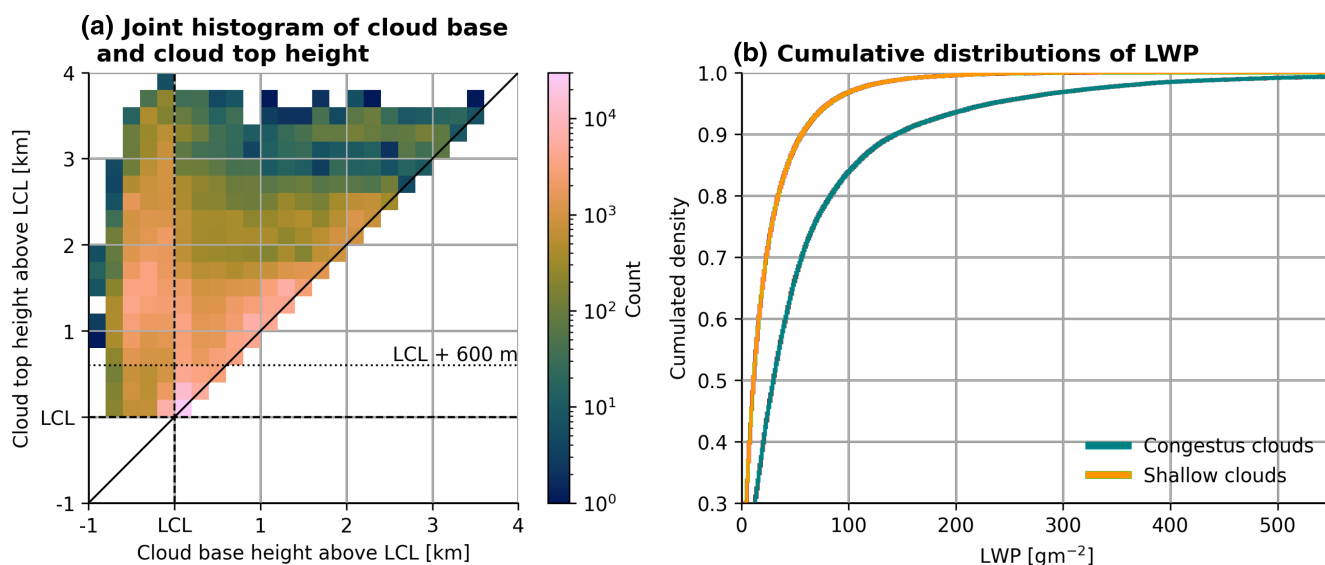

FIGURE 2   Distribution of cloud-top heights above the LCL and cloud-base heights for all clouds. The level LCL +600 m is used to distinguish shallow from congestus clouds. [Colour figure can be viewed at wileyonlinelibrary.com]

TABLE 2 Parameters of liquid water path, rain rate, cloud base, cloud-top height distributions: mean, median, standard deviation, 10th and 90th percentiles.

Variable	Mean	Median	Standard dev	10th	90th
LWP shallow [g $\cdot$ m^{-2}]	22.36	11.80	32.02	0.21	57.14
LWP congestus [g $\cdot$ m^{-2}]	59.67	30.33	94.55	0.57	144.92
Rain rate shallow [mm $\cdot$ h^{-1}]	0.11	1.7	3.25	0.3	6.5
Rain rate congestus [mm $\cdot$ h^{-1}]	0.28	0.8	5.61	0.1	7.4
Cloud base shallow [m]	677.19	655.00	168.60	475.00	895.00
Cloud top shallow [m]	890.44	857.17	284.22	648.47	1147.87
Cloud base congestus [m]	1337.21	1522.81	618.48	595.00	2215.00
Cloud top congestus [m]	2027.13	1926.44	564.31	1412.76	2861.15

TABLE 3 Cloud statistics of ship observations during the EUREC^{4}A campaign based on the cloud classification method introduced in this work and based on Jacob *et al.* (2020)'s results.

Cloud type	Number of samples	Percentage
No LCL, no data	1522	0.1%
Clear-sky conditions	506525	59.2%
Shallow clouds	75318	8.8%
Congestus clouds	179019	20.9%
Other clouds	92627	10.8%
Total	855011	100%

mainly range between 1 and 2 km from the LCL, and the cloud base can also be found below the LCL. Drawing a horizontal line of LCL+600 m separates the shallow cloud mode from the congestus mode.

Based on this definition of shallow and congestus clouds, we find that cloudy profiles do not dominate the sky, aligning with previous studies (Konow *et al.*, 2021; Nuijens *et al.*, 2009; Schnitt *et al.*, 2024). Applying our classification method, we find that the sky is clear approximately 60% of the time (Table 3). Shallow clouds are the rarest, occurring only 8.8% of the time, while deep clouds occur in 20.9% of the cases. With this classification, we have only 10% of the identified clouds that are not classified. More than 95% of the shallow clouds have LWP smaller than 100 g $\cdot$ m^{-2}. More than 80% show LWP values below 50 g $\cdot$ m^{-2} and scarcely precipitate (Figure 2b). At least 30% of the congestus clouds have LWP larger than 50 g $\cdot$ m^{-2}, and 10% of them LWP larger than 150 g $\cdot$ m^{-2}. If we consider the 100 g $\cdot$ m^{-2} value as a good threshold for precipitation, we find that almost all precipitation occurs in congestus clouds. Moreover, occurrences of shallow and congestus clouds coincide with the mean values of the cloud-cover diurnal cycle occurrences displayed for similar cloud classes in simulated LES runs at 300 m horizontal

resolution (Vial *et al.*, 2019). Interestingly, in our case, the most observed cloud type is not the shallow type, as noted by Lamer *et al.* (2015) at the Barbados Cloud Observatory (BCO: Stevens *et al.*, 2015). Rather, the congestus type prevails, possibly indicating that different cloud regimes may exist in the open sea and in the Southern regions, characterized by lower vertical extension of congestus clouds and lower amounts of cloudiness, possibly due to a different sub-cloud layer regime.

3.2 | Classifying cloud mesoscale patterns: methods for satellite image classification

To link the ship-based observations presented in this article to the observed mesoscale cloud organization over the area, we introduce here the satellite observations and the method we used to classify cloud scenes over the ship track.

Supervised neural network classifications using human labels have proven useful for investigating the behaviors of cumulus archetypes in prior satellite and surface observation-based climatological studies (Bony *et al.*, 2020; Schulz *et al.*, 2021; Vial *et al.*, 2021). We apply the so-called "human-labeling approach" to the ship-borne measurements aboard the *RV MSM*. The relative infrequency of alignment between manual, human-labeled organization types (Schulz, 2022) and the sampling of the *RV MSM* resulted in too few observations for statistically reliable conclusions about the type behaviors (see Figure 1a); more details about LWP and radar reflectivity profiles of the time stamps classified as human-labeled are provided in Figure S2a,b, respectively, in the Supporting Information).

The deep-learning method based on the self-supervision approach presented in Chatterjee *et al.* (2024) overcomes the difficulty of imposing only four distinct

classes on the diversity of the mesoscale organization patterns found in the trades, which causes the scarcity of human labels over the ship track documented in Figure 1a. Like other deep-learning approaches (Denby, 2023; Janssens *et al.*, 2021), it demonstrates the capabilities in classification of clustering, and additionally guarantees dissimilarity in the samples with self-supervision by classifying the entire spectrum of cloud organization patterns.

In this work, we exploit the results of the representation learning models developed in Chatterjee *et al.* (2024). For satellite analysis, we used the cloud optical depth (COD) product retrieved from *GOES-R* ABI (Schmit *et al.*, 2005). We use the Daytime Cloud Optical and Microphysical Properties algorithm (DCOMP: Walther & Heidinger, 2012) with COD at 2-km horizontal and 10–15 min temporal resolution, respectively. The chosen domain study is (5°N–20°N and 40°W–60°W), and the study period analyzed is between November and April for the years 2017–2021. More details on these choices can be found in Chatterjee *et al.* (2024). To label cloud mesoscale patterns in COD images, we used the classification in discrete classes obtained from the network N2. N2 is a self-supervised approach, where feature vectors in two branches capture information from the input crops, making the cross-entropy loss function converge when they are similar and diverge otherwise. A spherical k-means algorithm present only in the upper branch (see fig. 2 of Chatterjee *et al.*, 2023 for a visualization of the network) assigns a label to each crop based on how close the crop is to the class centroid. The lower branch instead uses the cosine similarity to reduce the crop's distance from the centroid. Through iterations, the network learns to assign crops that are similar to the same class. To assign a satellite image with resolution 256×256 pixels to each ship position, we cropped the satellite data at each time step so that the ship position is at the center of each satellite image. We then feed all the satellite images associated with the ship track into the network N1 primarily, and then into the network N2 to get a label generated by the network.

Chatterjee *et al.* (2024) characterize the classes using data from the Clouds and Earth's Radiant Energy System fourth Edition (CERES, Edition-4A: Wielicki *et al.*, 1996). Fig. 1 in Chatterjee *et al.* (2024) distributes all images in a 2D continuum derived with t–SNE (van der Maaten & Hinton, 2008), presenting the diversity of satellite scenes. While class 3 represents deep convective clouds with very high cloud fraction and water-vapor amounts, all the other classes represent shallow convection regimes with cloud fractions below 50%. More discussion on the classes is presented in Section 6 and in Supporting Information Section S5.

4 | CHARACTERISTICS OF SHALLOW AND CONGESTUS CLOUD SAMPLES

How do shallow and congestus clouds evolve when the amount of liquid water in the cloud increases? When does this evolution mainly take place during the day? Can we identify typical dynamical and thermodynamical conditions in which it is observed? Exploiting the cloud classification method explained in the previous section, we now analyze the evolution of macrophysical cloud properties in Section 4.1 by making use of the classified shallow and congestus radar reflectivity profiles as well as corresponding LWP measurements. Based on the measurement statistics, we analyze the daily cycle of cloud and marine boundary-layer properties in Section 4.2.

4.1 | Evolution of macrophysical properties

We track the shallow and congestus cloud evolution in the trades in a statistical sense by analyzing radar reflectivity and LWP observations for the entire collected dataset, as illustrated in Figure 3.

First cloud signatures occur for LWP values below $10 \, \mathrm{g \cdot m^{-2}}$, a value within the LWP observation uncertainty (Figure 3a: see Schnitt *et al.*, 2024). We identify two modes of cloudiness following the classifications. The shallow mode (grayscale contours) is near the limit of the radar sensitivity for Ze values between $-40 \, \mathrm{dBZ}$ and $-30 \, \mathrm{dBZ}$ and does not extend above 1000 m. The second mode is associated with congestus clouds, showing larger Ze values between -30 and $-20 \, \mathrm{dBZ}$, and is located between 1000 and 2000 m. The higher congestus reflectivity values might be due to a lower number of larger cloud droplets, which raise Ze values due to their proportionality to the droplet diameter to the sixth power. The first condensation of moisture patches into liquid cloud droplets occurs for LWP values between 10 and $100 \, \mathrm{g \cdot m^{-2}}$, corresponding to values previously found in LES studies (Bretherton & Blossey, 2017). For increasing LWP values up to $50 \, \mathrm{g \cdot m^{-2}}$ (Figure 3b), the shallow and congestus modes slant toward higher altitudes and slightly larger radar reflectivity values, indicating possible cloud droplet growth by diffusion of water vapor. Shallow and congestus peaks are still separated at $50 \, \mathrm{g \cdot m^{-2}}$. We hypothesize that the lower, shallow peak originates from the initiation of convection coupled to sub-cloud layer dynamics, while the upper, congestus peak relates to decaying cloud patches or trailing edges of deep clouds (Lamer *et al.*, 2015).

The patterns change for both congestus and shallow clouds for LWP between 50 and $300 \, \mathrm{g \cdot m^{-2}}$ (Figure 3c,d).
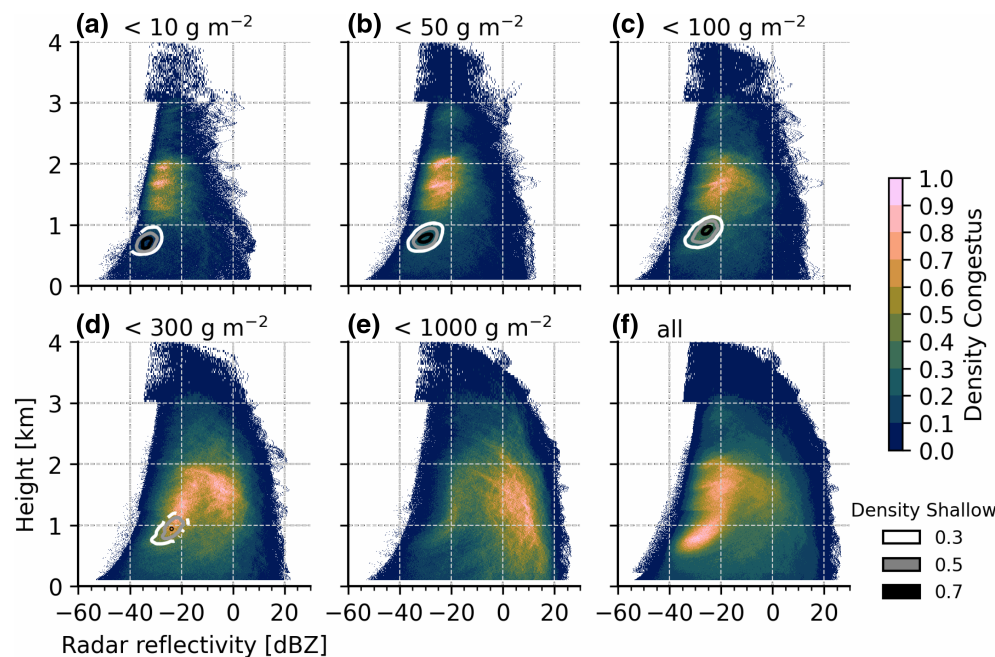
FIGURE 3 Normalized occurrence of radar reflectivity bins as a function of height for shallow (gray shaded contours) and congestus (blue to orange color shades), for different LWP regimes: (a) LWP $< 10 \cdot g \cdot m^{-2}$, (b) LWP $< 50 \cdot g \cdot m^{-2}$, (c) LWP $< 100 \cdot g \cdot m^{-2}$, (d) LWP $< 300 \cdot g \cdot m^{-2}$, (e) LWP $< 1000 \cdot g \cdot m^{-2}$, and (f) all radar bins together. [Colour figure can be viewed at wileyonlinelibrary.com]

For LWP $< 100 \cdot g \cdot m^{-2}$ (Figure 3c), we can identify a larger peak for congestus clouds extending up to 0 dBZ, while the detached peak for shallow clouds continues to grow by diffusion of water vapor, increasing in Ze slowly up to -20 dBZ and increasing slightly in elevation. Finally, for LWP > 100 and $< 300 \cdot g \cdot m^{-2}$ (Figure 3d), the shallow and congestus peaks get merged in a slanted mode extending from -20 around 1 km to -15 at 1800 m. This mode represents cloud droplets transported upwards by updrafts and growing by diffusion of water vapor in the lower heights and collision coalescence in the upper part of the cloud, between 1500 and 2000 m. In this height range, we have a large variability in Ze, ranging from -20 to 10 dBZ, indicating the presence of cloud and rain drops of different sizes. Between 1 and 2 km, we can identify two main peaks of reflectivity, one at -20 dBZ and the other one around -5 dBZ. The variability of the droplet sizes that we observe is a necessary condition for the collision–coalescence process to initiate the production of first rain stages, indicated by radar reflectivity larger than 0 dBZ (Figure 3e). Turbulence (Beheng, 2010; Grabowski & Wang, 2013) and giant cloud condensation nuclei (Feingold *et al.*, 1999) are the main mechanisms that play a role in broadening the cloud droplet size distribution and initiating collision coalescence in warm clouds. In our observations, we hypothesize that turbulence is the principal factor playing a role in these clouds, but more studies, involving in situ observations from the cloud kite on board, LES, and forward modeling, are needed to verify this hypothesis.

For LWP $> 300 \cdot g \cdot m^{-2}$ and $< 1000 \cdot g \cdot m^{-2}$, we mainly look at precipitating pixels characterized by Ze values between 0 and 20 dBZ spanning an area from 2000 m to the

ground (Figure 3e). Consistent with the results of Lamer *et al.* (2015), we find that non-precipitating clouds with LWP $< 100 \cdot g \cdot m^{-2}$ have an elevated high reflectivity core and a positive reflectivity gradient from cloud base to cloud top. In contrast, precipitating cumuli for larger values of LWP display a reflectivity core that does not peak at cloud top, but in the center of the cloud, with consequent change in the structure of the vertical gradient.

Figure 3f depicts the evolution of all profiles, including shallow and congestus clouds. For mean shallow clouds, the adiabaticity factor, given by

$$f_{\text{ad}} = \frac{LWP_{\text{obs}}}{LWP_{\text{ad}}},$$

is 0.26, indicating that, on average, shallow clouds are sub-adiabatic and contain less liquid water than we would expect in adiabatic conditions. They follow an adiabatic growth for Ze values smaller than -20 dBZ, and the transition from the adiabatic profile to larger reflectivities occurs between 1500 and 2000 m where collision and coalescence onset takes place, generating precipitation. We observe an increase in reflectivity from cloud base to cloud top of the order of 15 dBZ, consistent with previous observational studies (Ghate *et al.*, 2011).

Our results agree with the findings of Lamer *et al.* (2015), who identified a threshold of -20 dBZ to discriminate between non-precipitating cumuli and clouds in which particle sedimentation (from drops of size larger than 50 μm) starts to control the signal in the radar volume. Our radar has a smaller sensitivity due to its higher frequency compared with the 35-GHz

radar used in their study, but it is still sensitive enough to capture the variability in the clouds with reflectivities smaller than the −20 dBZ threshold. Based on these results, we can, thus, also think of shallow and congestus clouds as two consecutive stages of cloud formation and development. A shallow cloud can form when, at cloud base, ascending air motions arise from converging moisture advected by shallow mesoscale circulation patterns (George *et al.*, 2023; Janssens *et al.*, 2023; Janssens *et al.*, 2024; Narenpitak *et al.*, 2021). Also SST anomalies (Acquistapace *et al.*, 2022b; Chen *et al.*, 2023) or tropical instabilities (Bretherton & Blossey, 2017) can generate ascending moist patches that produce shallow clouds. Shallow clouds then form at LCL height and, given optimal conditions of updraft intensities and moisture anomalies, can grow further to congestus clouds to generate precipitation. To understand better the conditions in which the transition from shallow clouds to congestus clouds occurs, we investigate the thermodynamic and dynamic characteristics of the sub-cloud layer further in Section 5.

4.2 | Daily cycle of clouds and sub-cloud layer

The synergistic equipment of profiling instruments monitoring the boundary layer and the cloud properties allows us to gain insights into the diurnal cycle of clouds and their sub-cloud layer during January and February 2020.

Before analyzing the variability of all the variables, we consider the LCL (Figure 4e). LCL height (black curve) displays a clear diurnal cycle: it varies between 600 and 650 m at night and grows steadily after 0900 LT to values between 700 and 750 m. Then, after sunset (1830 LT (UTC-4h), it decreases back to the typical night-time values. Considering the variability of the LCL during the day, we opted for displaying the vertical variability of marine boundary-layer dynamics and clouds as a function of vertical distance from the LCL.

We first look at the diurnal cycle of shallow (Figure 4a) versus congestus clouds (Figure 4b), exploiting the relative occurrence of FMCW radar reflectivity profiles (Figure 4e). Shallow clouds occur with a hydrometeor fraction between 0.2 and 0.45 during the day without visible variability. This evidence agrees with the study of Kollias and Albrecht (2010), who show that marine boundary-layer clouds do not have an apparent diurnal cycle. Congestus clouds (Figure 4b) show more substantial fluctuations, displaying a higher occurrence between 0500 and 1600 LT, with a peak between 1200 and 1400 LT characterized by deeper clouds, probably including precipitation (Figure 4c). Interestingly, rainy profiles occur during the whole day with very similar hydrometeor fraction

amounts, while the non-rainy profiles are more variable in time and cloud geometrical thickness (Figure 4c,d).

Congestus non-rainy hydrometeor fraction shows significant variability in regard to vertical extension and height of the cloud top during the day (Figure 4d), with maximum cloud geometrical thickness between 0800 and 1600 LT. A weak increase in congestus, non-rainy cloud-top height (Figure 4d) is visible starting from 1800 LT until 0200 LT. Then, between 0200 and 0600 LT, cloud-top height stays constant at around 1500 m, but cloud geometrical thickness seems to reduce, partially recalling the cloud decaying found in LEM-300 m simulations (fig. 3b of Vial *et al.*, 2019). However, while, in their work, the decay extends until 1200 LT, in our observations, after 0600 LT, cloud-top height increases slightly again, resulting in vertically more extended cloud profiles. After sunrise and during the morning, congestus cloud amounts range between 0.3 and 0.4, and a first maximum appears at around 1600 LT, followed by another at 2000 LT, in contrast with the clear minima between 0900 and 2000 LT in cloud cover that appear in Vial *et al.* (2019)'s study for congestus non-rainy clouds. Congestus rainy hydrometeor fraction profiles (Figure 4c) show intense variability in cloud top from 1000 to 2200 LT, while hydrometeor cloud-top height is more homogeneous between 2200 and 1000 LT. The highest values of rainy hydrometeor cloud fractions lie between 1200 and 2200 LT.

When looking at the relative occurrence of shallow and congestus clouds (Figure 4e), shallow clouds show very little variability during the whole day, instead of maximizing during daytime as in Vial *et al.* (2023), while congestus clouds seem to be consistent with the maximization at night they show. The relative occurrence of rainy congestus cumulus clouds decreases after 0800 LT to reach its minimum at 1000 LT and then decreases until 1900 LT (Figure 4c). It thus seems that the highest values of hydrometeor cloud fraction visible in Figure 4c are caused by the fewer rainy clouds observed in the afternoon, possibly indicating more organized cloud systems resulting in higher hydrometeor fractions.

To investigate possible correlations between dynamical and thermodynamical sub-cloud layer conditions and cloud behavior, we make use of the ARTHUS and wind Doppler lidar measurements. Since these observing systems have a blind zone due to lack of overlap below 250 m (see Section 2.2), the part of the sub-cloud layer closest to the surface was not observed (gray hatched areas in Figure 4f–j), where the undulating behavior is caused by the LCL variability during the day.

While we did not find a clear signature in the diurnal cycle of the vertical wind (and thus did not report it in the figure), air temperature (Figure 4f) and water-vapor mixing ratio (Figure 4g) show a clear signature connected
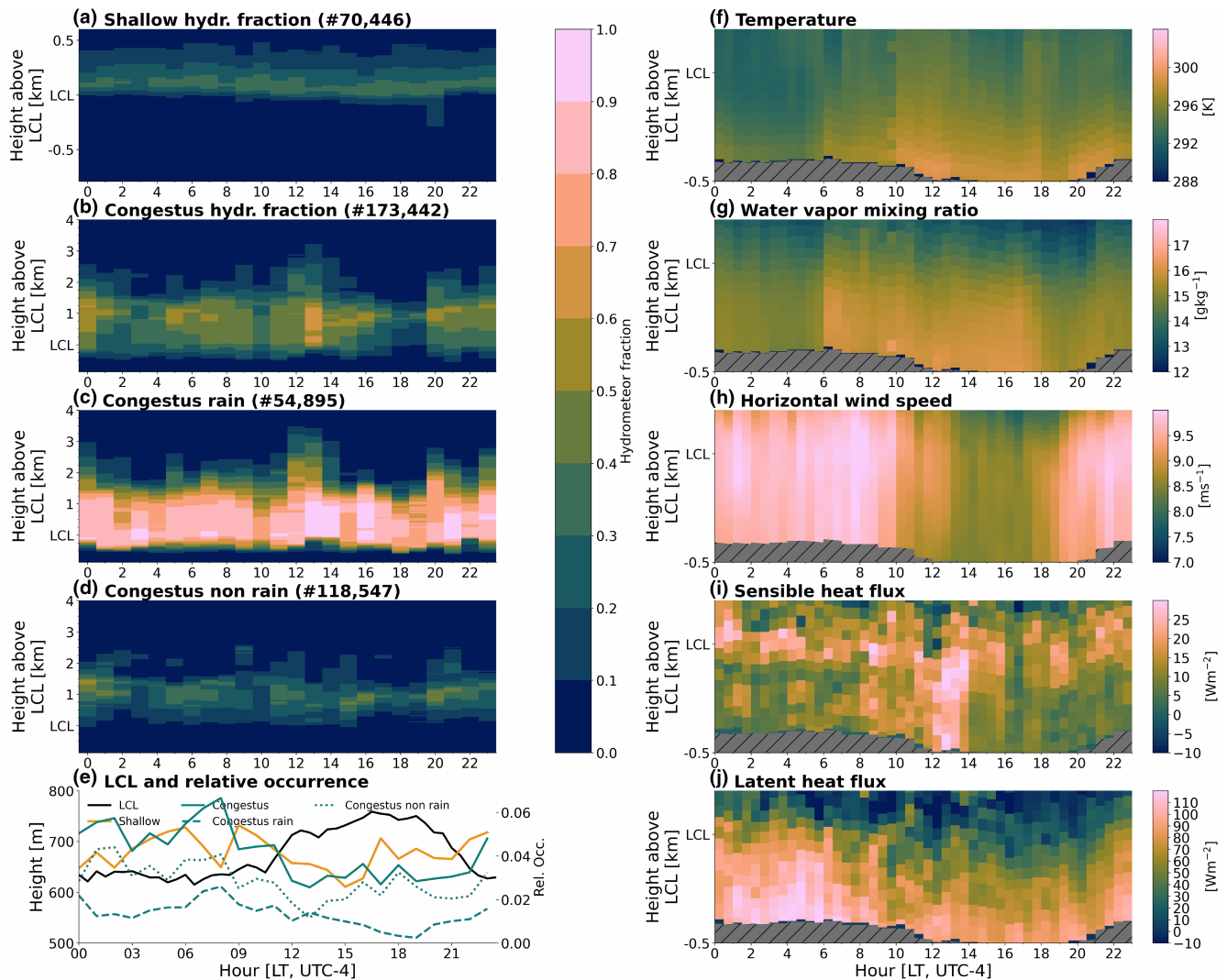
FIGURE 4   Diurnal cycle of (a) shallow hydrometeor fraction, (b) congestus hydrometeor fraction, (c) fraction of congestus clouds generating rain at the surface, (d) the same for congestus non-rainy profiles, and (e) LCL diurnal cycle as a function of height and relative occurrence of each cloud class. Moreover, in the right column and for the sub-cloud layer, diurnal cycles of (f) temperature, (g) water-vapor mixing ratio, (h) horizontal wind speed, (i) sensible, and (j) latent heat fluxes are shown. [Colour figure can be viewed at wileyonlinelibrary.com]

to sunrise (0630 LT) and sunset (1830 LT). Some anomalous cooler temperatures are detected between 1800 LT and 1900 LT in the layers closest to the sea surface, possibly due to sensor issues in the twilight zone. In the central part of the sub-cloud layer around 300–400 m elevation, the temperature rises initially by 1–2 K from sunrise to 1000 LT, and then warms the sub-cloud layer up to 4 K from the surface up to a distance of 250 m from the LCL until 1300 LT. This increase also corresponds to an increase of 3–4 g · kg^{-1} in water-vapor mixing ratio in the sub-cloud layer, possibly related to the evaporation of seawater. This relates to the sun warming the ocean surface, causing an increase in sensible heat flux of 10–20 W · m^{-2} (Figure 4i).

All these variables suggest the initiation of moist buoyancy, with locally small, random updrafts and

downdrafts without clear signatures in the vertical wind at the scale of our ship observations. However, these fluctuations reduce the horizontal wind speed by 1–2 m · s^{-1}, as well as the proportional latent heat flux by approximately 30 W · m^{-2} (Figure 4j). Both the intensity of the wind speed and its positive gradient with height in the sub-cloud layer correspond to lidar observations at BCO during EUREC^{4}A, as well as European Centre for Medium-Range Weather Forecasts (ECMWF) atmospheric reanalysis fifth generation (ERA5) columns (fig. 5c of Savazzi *et al.*, 2022). By comparing the diurnal cycle variation of the horizontal wind speed found here with the lidar observations in Savazzi *et al.* (2022), we find up to 2 m · s^{-1} reduction in wind speed between 1000 and 2000 LT compared with the reduction of approximately 1 m · s^{-1} in wind lidar

observations, ERA5, and forecasts shown in fig. 7c of Savazzi *et al.* (2022). However, in this work, the horizontal wind speed is not corrected for the ship velocity, and the statistic relies on the fact that, for a large sample of data, ship velocities can be distributed randomly across all time stamps and do not impact the diurnal variability observed. However, we do not consider the horizontal wind speed further in the analysis, because the hypothesis of no impact might fail when considering smaller subsets of data.

Finally, the time correlation between the moist buoyancy maximum and the increase in cloud depth occurring between 1200 and 1400 LT suggests a possible coupling between the sub-cloud layer thermodynamics and the change in cloud macroscopic properties. Similar correlations induced by anomalies in the sea-surface temperatures were observed in Acquistapace *et al.* (2022b). The analysis presented revealed a diurnal cycle in almost all the observed variables; the observed variability is larger than the one due to latitude presented in Figure 1. Thus, when possible, for characterizing the sub-cloud layer in the following sections, we look at anomalies relative to the daily cycle for all except cloud variables, to exclude the possibility that the variability seen could be due to daily variations.

5 | DYNAMICS AND THERMODYNAMICS OF CLOUD AND PRECIPITATION EVOLUTION

When shallow and congestus clouds form, how do the dynamic and thermodynamic fields deviate from the mean states observed in Figure 4? In Section 5.1, we investigate how different dynamic and thermodynamic conditions of the marine boundary layer initiate condensation and deepen the cloud layer. Once precipitation is initiated, how much rain falls, and how does it impact the sub-cloud layer? We then explore the thermodynamic and dynamic effects on the boundary layer in Section 5.2.

5.1 | Cloud and precipitation initiation

Convection initiation and sub-cloud layer thermodynamics and dynamics are tightly intertwined. The distribution of cloud bases for shallow clouds peaks around the LCL height, with a variability of approximately 500 m (Figure 5a and Table 2), which reflects the variations observed in the LCL during the day (Figure 4e). Congestus clouds, in contrast, display a bimodal distribution of cloud bases, with a minor peak around the LCL and an upper peak located around 1000 m from the LCL. The bimodal cloud-base height distribution corresponds to previous findings in Lamer *et al.* (2015), Jacob *et al.* (2020), and

Albright *et al.* (2023). Lamer *et al.* (2015) relate the elevated cloud base peak to clouds limited by the trade inversion, and attribute it to precipitating clouds with attached stratiform outflow.

The profiles of the median of the vertical velocity w (Figure 5b) as retrieved by the Doppler wind lidar reveal details of the dynamical conditions associated with cloud formation. The other percentiles for vertical velocity, as well as for the specific humidity and virtual potential temperature, are displayed in Figure S4 of the supplementary material. In the sub-cloud layer, in shallow non-precipitating conditions (orange solid line), a positive vertical wind of $0.1\,\mathrm{m\cdot s^{-1}}$ pushes the humid sub-cloud air to rise. In shallow non-precipitating conditions, the sub-cloud layer is the moistest, with $1\,\mathrm{g\cdot kg^{-1}}$ more moisture than clear-sky profiles in the sub-cloud layer (Figure 5c); cooling associated with updrafts causes condensation at the LCL (Figure 5d). We can see an increase in θ_v of up to 2 K at the LCL due to latent heat release. This buoyancy might be supported by air convergence through mesoscale circulations in cloud and sub-cloud layers. Positive w values are not present in the congestus clouds, since they represent a later stage of cloud development in which condensation and collision coalescence have already started in the cloud layer. Congestus non-precipitating clouds (solid cyan) show zero values of w from the LCL upwards, and values within $-0.1\,\mathrm{m\cdot s^{-1}}$ from the LCL to the ground. For congestus precipitating cases (dashed cyan, also detailed in section 5.2.2), downdrafts decrease in intensity towards the ground: we observe values of $-0.2\,\mathrm{m\cdot s^{-1}}$ at 300 m above the LCL that reduce to zero when approaching the ground, probably due to precipitation evaporation.

The positive anomaly in w is also found in the moistest quartile of LES profiles in fig. 8 of Bretherton and Blossey (2017). Their article investigates the aggregation of shallow cumulus convection at the mesoscale, and it can be related, in our observations, to the transition we hypothesize to see between shallow and congestus clouds. They find a positive anomaly of $0.02\,\mathrm{m\cdot s^{-1}}$ that extends progressively to higher elevations from hour 8 to hour 32 of the simulation. However, in the shallow stage, we cannot identify the dipole structure found in the simulations, characterized by a negative w anomaly above 850 hPa. Beyond the positive anomaly in the sub-cloud layer, we instead observe a negative anomaly in vertical velocity, completing the dipole structure predicted by Bretherton and Blossey (2017) in the more mature stages of congestus cloud precipitating.

Based on observational analyses, Lamer *et al.* (2015) highlight that the initial shallow, non-precipitating convection stage is characterized by consistent positive updrafts (their fig. 5, top left panel), which reduce in more
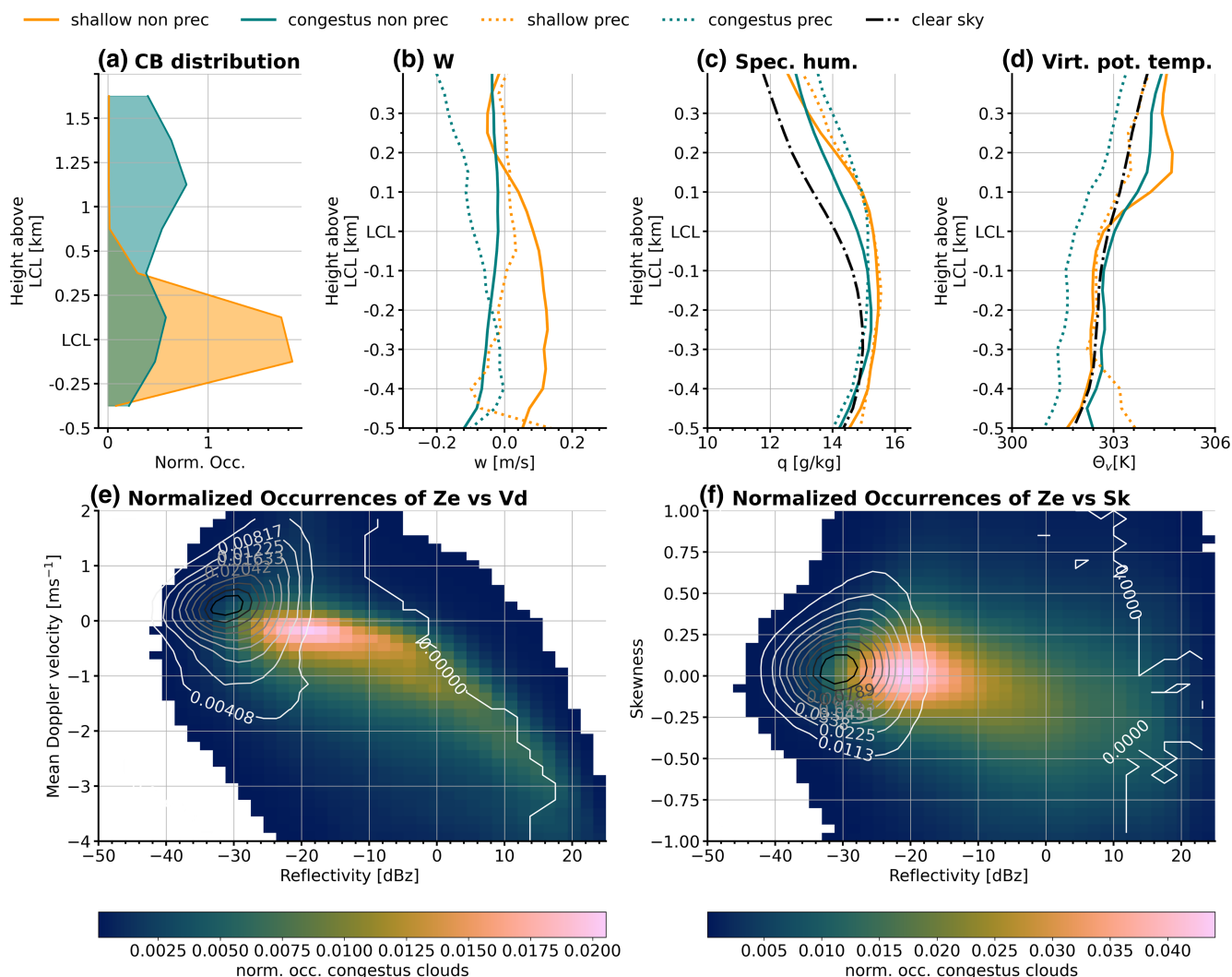
FIGURE 5 Boundary-layer conditions associated with the formation of shallow and cumulus clouds: (a) distribution of cloud-base heights for shallow (orange) and congestus (green); (b) vertical velocity profiles for precipitating (dotted) and non-precipitating (solid) shallow (orange) and congestus (green) profiles; the same for (c) specific humidity and (d) virtual potential temperature, but also displaying the corresponding profiles in clear-sky conditions (black dash–dotted line); only considering FMCW radar range gates in the cloud, normalized occurrences of (e) radar reflectivity (Ze) and mean Doppler velocity (Vd) and (f) radar reflectivity Ze and skewness Sk, for shallow (contour lines) and congestus (color-filled contours). [Colour figure can be viewed at wileyonlinelibrary.com]

mature stages of convection. This is in agreement with our findings for the shallow and congestus stages. Analyzing radar observations inside the cloud, we see that most of the shallow cumulus radar pixels display small values of reflectivity between -40 and -25 dBZ (solid contours, Figure 5e). Coinciding mean Doppler velocity values between 0 and $1\,\mathrm{m}\cdot\mathrm{s}^{-1}$ indicate the presence of updrafts in the cloud, in agreement with Lamer *et al.* (2015).

An additional piece of information on the formation of larger droplets generating precipitation is added by the skewness (Kollias *et al.*, 2011; Luke & Kollias, 2013; Figure 5f). The solid contours indicate that skewness values tend to be positive for shallow clouds, suggesting the onset of droplet sedimentation (Acquistapace *et al.*, 2019).

For congestus clouds (colored contours), skewness values are distributed symmetrically around zero for droplets with reflectivities between -25 and -10 dBZ. Skewness gradually turns negative for reflectivity values larger than -10 dBZ, indicating the formation of larger drops in the cloud and the onset of precipitation via collision–coalescence. In precipitation conditions, we expect precipitation to advect air downward when falling, which might cause a negative anomaly in vertical velocity in the air, as discussed previously. Based on the in-cloud radar measurements, we can see that congestus clouds (colored contours, Figure 5e) typically display mean Doppler velocity values ranging from 0 to $-3\,\mathrm{m}\cdot\mathrm{s}^{-1}$ for Ze values larger than -25 dBZ.

We further contrast thermodynamic conditions associated with shallow and congestus clouds. Specifically, we compare the specific humidity q and the virtual potential temperature θ_v profiles in precipitating and non-precipitating shallow and congestus clouds, respectively, with the profiles obtained in clear-sky conditions (Figure 5c,d). Albright *et al.* (2023) displayed the clear-sky profiles of q and θ_v nicely to characterize the transition layer (their fig. 3), namely extending from 500 to 700 m. By looking at observed clear-sky profiles here, we also observe a transition layer characterized by a specific slope in q and θ_v profiles that extends approximately from 100 m below the LCL to 100 m above the LCL. Considering LCL variability due to the diurnal cycle, this corresponds to heights from 500–600 m to 700–800 m, which is in rough agreement with their results.

Below the LCL, q in clear-sky conditions is almost constant and has a mean value of 14.4 g·kg^{-1}. Also, the mean profile of θ_v is almost constant below the LCL, displaying a value of 302 K in the sub-cloud layer, 1 K warmer than the dropsonde observations in Albright *et al.* (2023) (probably related to calibration bias). We only see some deviations in both q and in θ_v around -500 m from the LCL, where we could have observation errors, because this region might fall below the overlap zone (250 m) of the ARTHUS Raman lidar (see Section 2.2).

In non-precipitating congestus conditions (solid green), q reaches a maximum of 15.6 g·kg^{-1} between -375 and -250 m; then, it decreases towards the LCL. In clear-sky conditions, q is reduced at the same height to 14.8 g·kg^{-1}. Correspondingly, θ_v shows larger values than for clear-sky conditions, suggesting that condensation might already have started at this elevation. The reduction of q can be due to clouds starting to form, as confirmed by the co-located peak in congestus cloud base. We observe an increase in θ_v and a strong reduction in q occurring above the LCL. They might be connected with condensation taking place around the LCL for shallow clouds, even if some cloud bases also occur below the LCL, as can be seen in Figure 5b.

Finally, shallow and congestus profiles (both precipitating and non-precipitating) are (Figure 5d) moister and (Figure 5e) warmer than clear-sky cases, a condition we will also observe in the next sections. If we look at precipitating congestus clouds (dashed green), θ_v is colder than the clear-sky θ_v by 0.5 K across the entire sub-cloud layer. We hypothesize that this reduction might be due to rain evaporation cooling the environment by taking up energy from the air to release water vapor. In this case, however, we expect an increase in q, which we do not observe. As will be argued later, we hypothesize that the increase in water vapor is counterbalanced by the fact that congestus precipitation is advected, as can also be seen in Figure 5b)

through dry cold air descending from upper layers to the sub-cloud layer. As the lidar observations and retrieval are impacted by rain, we cannot consider the q profile above the LCL as representative in congestus precipitation conditions (green dashed line in Figure 5d).

5.2 | Impact of precipitation on boundary-layer properties

How often do we have rain in the trades? How often does virga occur compared with precipitation reaching the ground? How do virga and precipitation impact the marine boundary layer? To tackle some of these questions, we looked at precipitation rain rates from the weather station attached to the FMCW radar, and the vertical extension of virga depths, which we defined as the vertical distance in meters between the cloud base and the last radar reflectivity bin of the FMCW radar vertically detected signal (Figure 6). In Section 5.2.1 we look mainly at virga and light precipitation characteristics and how these impact the sub-cloud layer, while in Section 5.2.2 we focus on precipitation and cold pools.

5.2.1 | Virga and light precipitation

When shallow clouds precipitate, rain rates are typically below 5 mm·h^{-1}. This result is in agreement with previous works from Nuijens *et al.* (2009), who show no rain rates above 10 mm·h^{-1}, with most of the distribution lying below 1 mm·h^{-1}, as in our case for both shallow and congestus clouds. However, not all precipitation reaches the ground: Kalesse-Los *et al.* (2023) found that 42% of the clouds detected from the *RV Meteor* during EUREC^{4}A were producing precipitation evaporating before reaching the ground. In the presence of shallow clouds, virga depths, defined as the vertical extension of precipitation before it evaporates, scarcely exceed 400 m (Figure 6a). Thus, shallow clouds have thin virga layers that evaporate a few hundred meters below the cloud base. In the case of congestus clouds instead (Figure 6b), virga depths range between 200 and 800 m and thus contain a much larger amount of liquid water to evaporate.

When evaporation takes place, the small raindrops take up energy from the sub-cloud layer to become water vapor, making the layer cooler (negative anomaly) and moister (positive anomaly) in the vicinity of the virga. For shallow clouds, this process occurs in the sub-cloud layer below the cloud base independently of the depth of the virga (Figure 7a,c). Interestingly, virga drops are not large enough to generate downdrafts visible as anomalies in the vertical velocity field (Figure 7e). Thus, the process
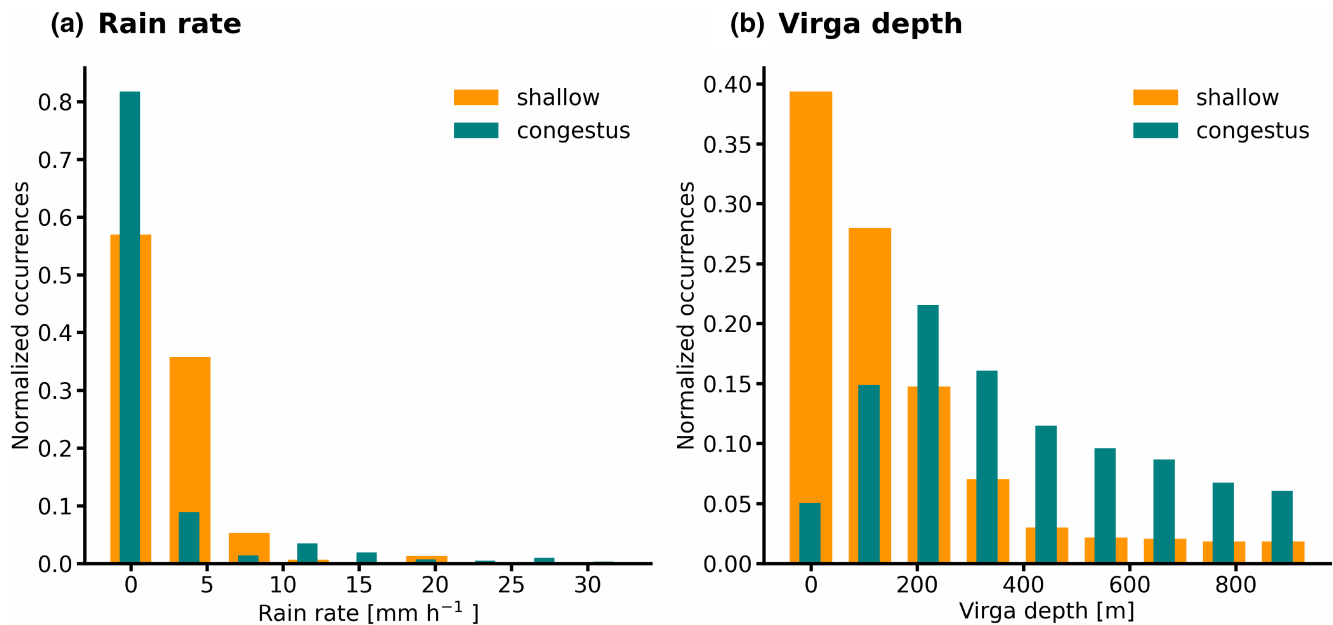
FIGURE 6 Distribution of (a) surface rain rates and (b) virga depths for shallow and congestus cumulus clouds. [Colour figure can be viewed at wileyonlinelibrary.com]

does not deplete the positive anomaly in vertical velocity that we observed in shallow non-precipitating clouds (Figure 5c), which is also visible in the sub-cloud layer in Figure 7e.

In the presence of congestus clouds (Figure 7b), we observe a positive temperature anomaly field that characterizes the congestus conditions. The environment in congestus conditions is more humid and warmer than in clear-sky conditions (see also Figure 5c,d), as also proven by radiosoundings (see Figure 8). We expect that the mean temperature state with respect to which we calculate the anomalies will be determined mainly by clear-sky conditions, present 60% of the observing time (see Table 3). However, the sub-cloud layer presents a patch of colder and drier air (see Figure 5b,d), for virga depths of 200–400 m, that might originate from upper layers that are drier and colder than the sub-cloud region and might have been advected there by cold pools associated with rain. It is plausible to observe the cold-pool current below the virga, because virga typically occurs at the edges of the precipitating cloud system, where the cold-pool current might start spreading horizontally. Grandpeix and Lafore (2010) already found that downdrafts associated with precipitation entrain dry, cool air. We hypothesize that the same process is taking place here: the anomalies in the vertical velocity for virga in congestus clouds (Figure 7f) change signs in the sub-cloud layer for increasing virga depths. For lower virga depths, the subtle updrafts are still sustaining the cloud development, but we see downdraft motion taking place in the case of deeper virga. Zuidema *et al.* (2011) observed a similar behavior during the ship portion of the

RICO campaign in an area slightly north of the one sampled during this campaign (Prof. Dr. Zuidema, personal communication, 2024).

5.2.2 | Stronger precipitation and cold pools

We now look more in depth at more intense precipitation processes, to verify whether stronger rain events entrain dry and cold air from cloud-top regions. We look at the radiosoundings launched in the presence of congestus and shallow cloud cases. We check the variability of the equivalent potential temperature and specific humidity anomaly as a function of height (Figure 8) to verify our hypothesis with an independent dataset. We look at all precipitation cases without restricting ourselves to virga only. As a reference, we consider the clear-sky conditions and calculate anomalies of q with respect to clear-sky cases for shallow and congestus precipitating and non-precipitating. Each radiosonde is labeled using the cloud classification we adopted based on the classification label assigned when it was launched from the *RV MSM*.

Shallow clouds (Figure 8a) display an equivalent potential temperature (θ_e) profile very similar to the clear-sky case (dashed line). Both profiles show a well-defined mixed layer in the lowest 500 m, above which the temperature decreases in the cloud layer. The lowest height of cloud base for shallow clouds corresponds to 500 m (light-gray histogram). Also, regarding specific humidity anomalies with respect to clear-sky cases (colored lines), anomalies vary within
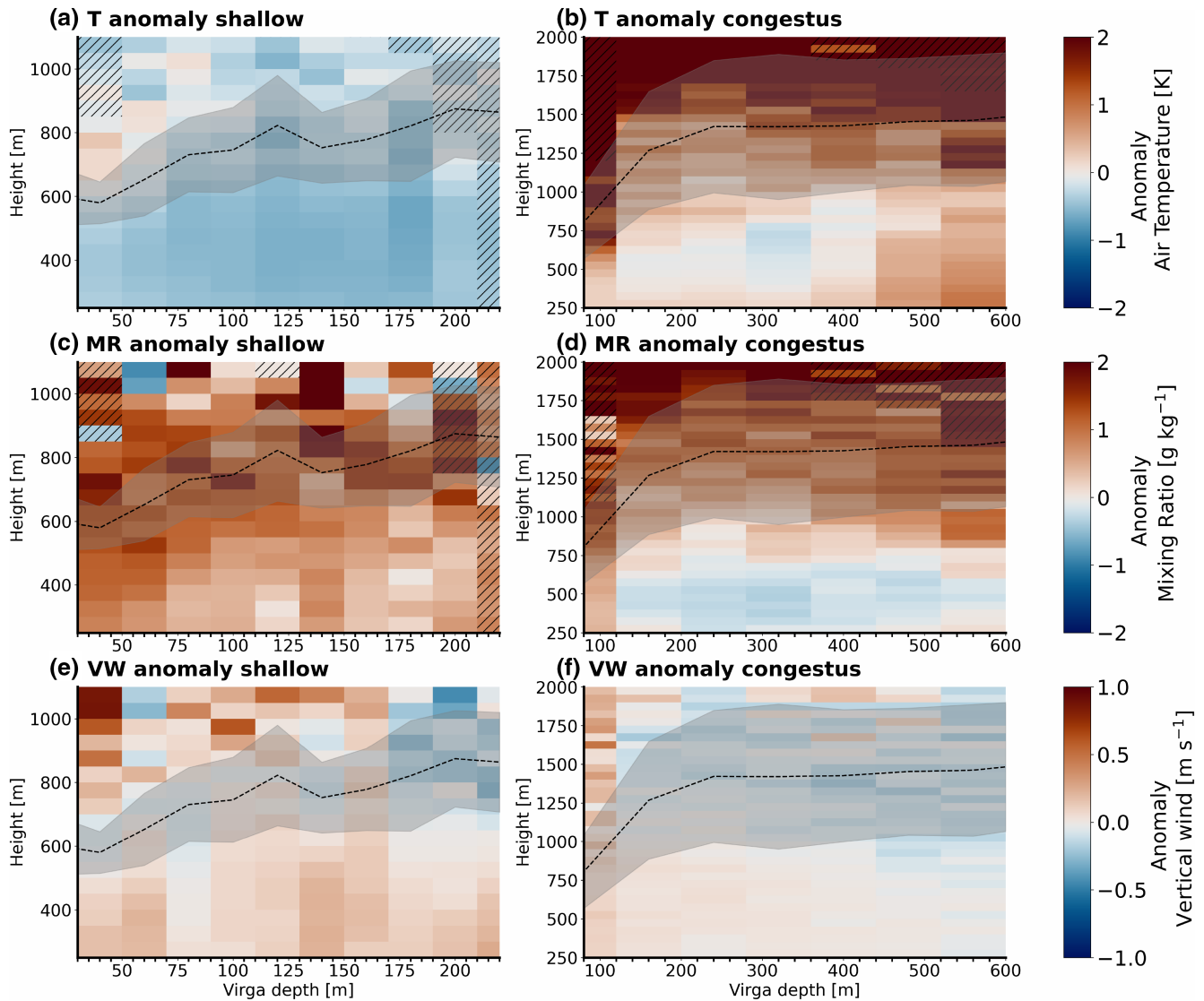
FIGURE 7   Air temperature, mixing ratio, and vertical wind anomalies calculated for (left) shallow and (right) congestus clouds in virga conditions. Hatched areas correspond to regions where mean fields are derived using fewer than 30 samples, and are thus considered not representative. The mean (dashed) and standard deviation (gray area) of the cloud-base height as a function of virga depth are overplotted. [Colour figure can be viewed at wileyonlinelibrary.com]

$1 \, g \cdot kg^{-1}$. Unfortunately, no soundings were launched in shallow-cloud precipitation conditions. Therefore, we have no information on precipitating shallow clouds.

Congestus non-precipitating clouds (thin colored line in Figure 8b) display a profile characterized by warmer air compared with clear-sky cases in the sub-cloud layer below 500 m. Above this height, the equivalent potential temperature decreases approximately up to the lower edge of the distribution of congestus cloud-base heights (dark gray histogram in the figure). From that height at around 1000 m up to 3000 m, θ_e seems to maintain a constant value of around 337 K, indicating a well-mixed cloud layer, possibly due to efficient mixing due to convection, 3–5 K warmer than the clear-sky profile. The profile for congestus non-precipitating clouds is similar to that obtained for

cold-pool cases in fig. 11a of Touzé-Peiffer et al. (2022). They find that cold-pool θ_e profiles are also well mixed around 337 K between 1000 and 3000 m. Specific humidity for the non-precipitating congestus profile has $1 \, g \cdot kg^{-1}$ positive anomaly in the sub-cloud layer. In contrast, the cloud layer, especially between 1000 and 3000 m, is up to $3 \, g \cdot kg^{-1}$ more humid than the clear-sky case.

However, conditions change when we consider congestus precipitating clouds: in the sub-cloud layer, the temperature profile appears well mixed and approximately 1 K colder than the clear sky, as in Touzé-Peiffer et al. (2022). However, in the lowest 150 m it becomes 1 K warmer, coinciding with the clear-sky profile case. We are not sure that this signal, so close to the surface, is reliable (see discussion on *RV MSM* radiosoundings in Stephan et al., 2021).
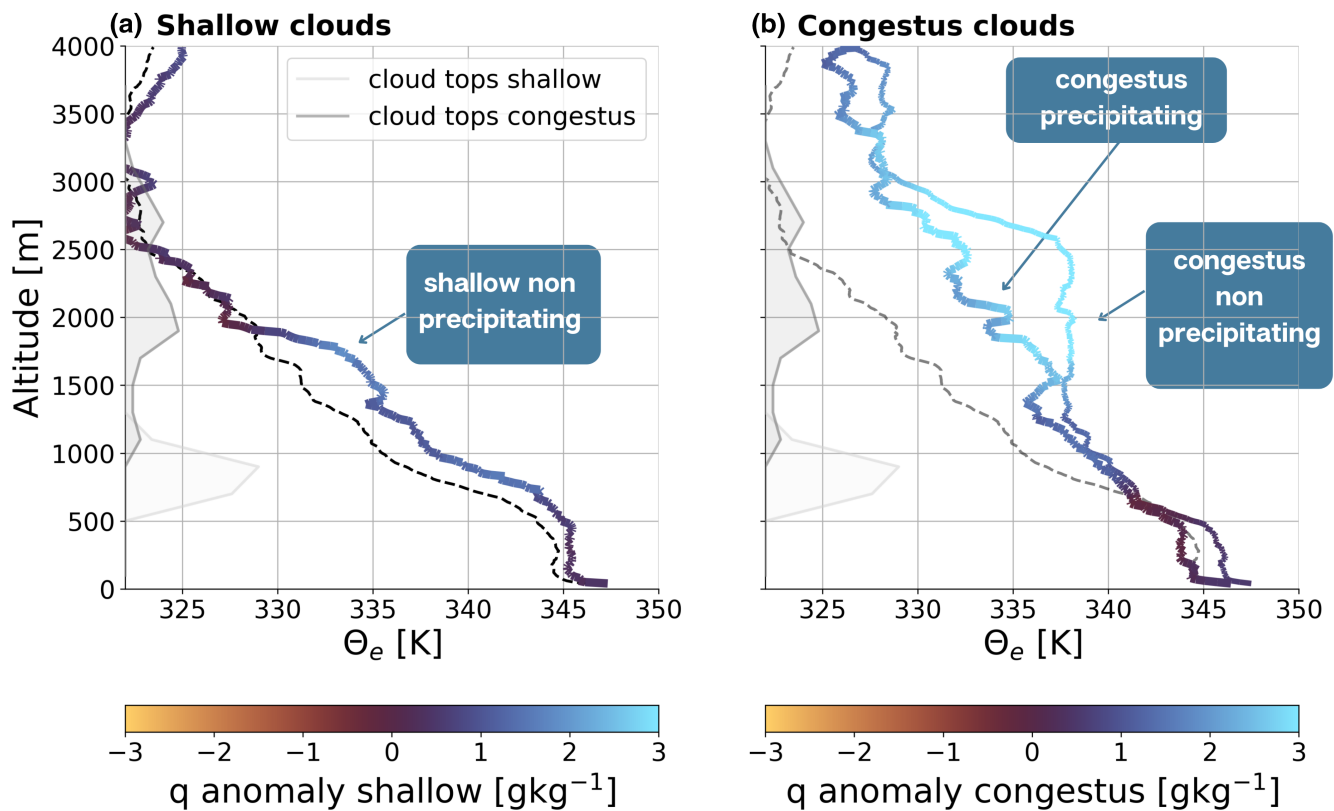
FIGURE 8 Mean profiles of equivalent potential temperature θ_e obtained from radiosondes launched from the *RV Maria S. Merian* in clear-sky conditions (black dashed line) and in the presence of shallow non-precipitating clouds (thin line), congestus non-precipitating (thinnest line), and precipitating clouds (thickest line). No soundings were launched in the presence of precipitation from shallow clouds. Colors represent the specific humidity anomaly of each profile relative to the specific humidity in clear-sky conditions. Cloud-top height distributions obtained from FMCW radar reflectivity observations at the time of radiosonde launch for shallow and congestus clouds are reported, for reference, in shades of light and dark gray, respectively. [Colour figure can be viewed at wileyonlinelibrary.com]

One possible explanation might be the presence of rain reaching the ground and inducing a displacement of moist and warm air that was there before the rain initiated, as suggested in Langhans and Romps (2015) (see their fig. 4, stage 2). In the cloud layer, the precipitating congestus profile shows more substantial variability in θ_e compared with the non-precipitating one, with values of θ_e lying in between clear-sky and congestus non-precipitating cases but still stably warmer than clear-sky cases, as we found in Figure 7b. Moreover, despite being still in a moister environment compared with clear-sky conditions, the precipitating profile shows a lower positive anomaly than the non-precipitating one. In other words, the air in rain conditions is drier and colder than in non-precipitating congestus conditions. This result is because rain, while falling, advects air from upper layers that are drier and colder than the cloud layer before the rain starts. This evidence confirms our previous analysis (Figure 7b) and also what was found in other modeling and observational studies (Grandpeix & Lafore, 2010; Zuidema *et al.*, 2011).

Most of the rain rates larger than 5 mm · h^{-1} are due to congestus clouds (see Figure 6) and are often connected

to cold pools. To investigate the impact of more intense precipitation, we collected 86 rainy events with precipitation reaching the ground and used the algorithm to detect cold pools developed by Vogel *et al.* (2021) to extend their analysis through characterizing the whole sub-cloud layer vertical structure. The onset of the cold-pool event is represented by t_{max}. The time of the minimum temperature reached during the cold pool is t_{min}. If we consider the time between t_{max} and t_{min} as indicative of the duration of the rain event, 80% of the cases show durations below 22 minutes and a median slightly larger than 15 minutes, roughly in agreement with Vogel *et al.* (2021) (see Figure S3 in the supplementary material). Remote-sensing observations from ARTHUS and Doppler lidars in rainy conditions are challenging. We compared them with radiosoundings launched in precipitating and non-precipitating conditions to verify their reliability. To compile these statistics, we removed all lidar profiles occurring in rainy conditions, as identified with cloud radar data. We observed that, within the sub-cloud layer, there is a substantial agreement between radiosondes and ARTHUS-based profiles selected by this procedure (see Figure S1 in the supplementary

FIGURE 9 Mean anomalies of (a) surface air temperature and (b) surface relative humidity. We also display (c) the mean FMCW radar reflectivity, and then anomalies of (d) mean vertical wind speed, (e) mean temperature, and (f) mean water-vapor mixing ratio as a function of time, from 60 minutes before t_{max} (onset of the cold pool) and 60 minutes after t_{min} (minimum temperature induced by the cold pool at the surface). [Colour figure can be viewed at wileyonlinelibrary.com]
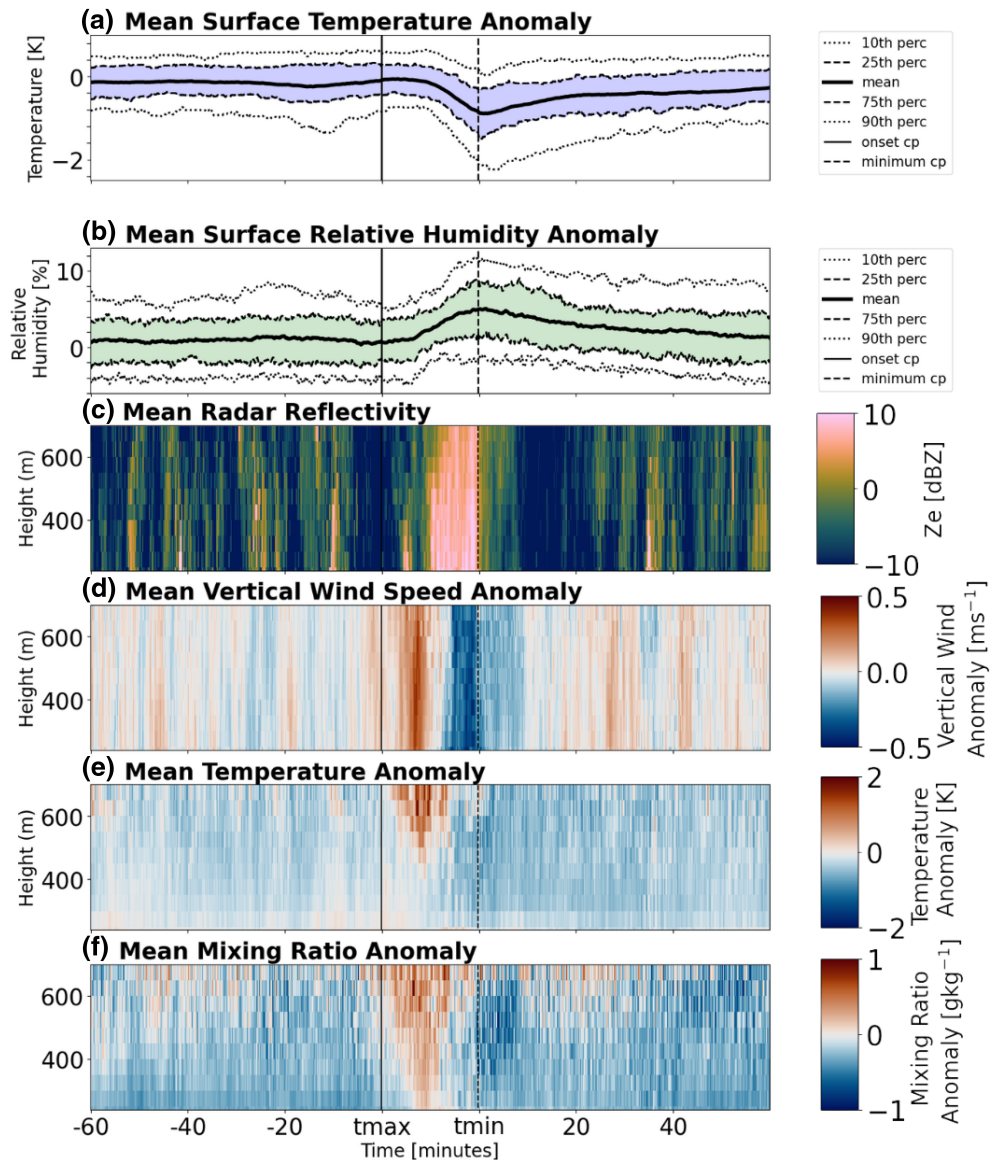
material for details), which allowed us to produce this analysis.

On average, mean surface temperature anomalies (Figure 9a) induced by the cold pool in the minimum detected temperature do not exceed 1°C, while in Vogel *et al.* (2021) they reached 1°C. This is potentially due to their larger number of cases. We observe a 5% positive variation in relative humidity (Figure 9b) at the surface when the minimum temperature is reached, in agreement with Vogel *et al.* (2021). Also, the qualitative behavior of the variation of surface air temperature and relative humidity resembles what is shown in their fig 3a,d, confirming that the approach presented is consistent. The maximum amount of precipitation, with radar reflectivity values larger than 10 dBZ, occurs between the onset of the cold pool and the minimum temperature t_{min} (Figure 9c). It decreases dramatically after t_{min}, first at the surface and then also below cloud base, possibly

indicating the presence of virga and evaporating precipitation in the external parts of the clouds that are further from the precipitating cloud core. Precipitation is anticipated by strong homogeneous updrafts in the whole sub-cloud layer (Figure 9d), causing vertical velocity anomalies that initiate at t_{max}, then intensify up to $0.5 \, \text{m} \cdot \text{s}^{-1}$, and then decrease before t_{min}, to leave space for the rain, associated with strong downdrafts of $-0.5 \, \text{m} \cdot \text{s}^{-1}$ anomaly.

From the cold-pool updrafts, downdrafts, and precipitation, we notice some interesting patterns in temperature (Figure 9e) and mixing-ratio (Figure 9f) anomalies that confirm our previous analysis. At around 500 m, during the updraft, we see a positive temperature anomaly of +2°C, which can be due to the heat released during condensation of water vapor advected up by the vertical wind. When the downdraft sets in, we can see that the positive temperature anomaly ceases, and, from t_{min} onwards, a clear negative temperature anomaly of around −1°C is

present in the sub-cloud layer from 400 to 700 m. This anomaly seems to be due to evaporating rain (see virga in the same region in the radar reflectivity, Figure 9c), which is taking energy from the environment to convert liquid water to vapor, as seen in Figure 7b,d. However, it might also indicate the presence of cold and dry air advected in the sub-cloud layer by precipitation. Unfortunately, the signal is noisier in rainy conditions than in virga conditions, and overlap issues and rain contamination might affect values closer to the surface. Between t_{max} and t_{min}, in correspondence with the stronger updrafts, there is a positive anomaly of the mixing ratio of between $+0.5$ and $+1\,g\cdot kg^{-1}$ that might be due to the convergence of moist air at the updraft base. This patch of humidity is also described in Langhans and Romps (2015) as a pre-rain water-vapor anomaly. In our observations, we can hypothesize that it can be created dynamically by the convergence of air masses in the sub-cloud layer towards the updraft region, as observed in mesoscale circulations (George et al., 2023). After t_{min}, we notice a negative anomaly of up to $-1\,g\cdot kg^{-1}$ in the sub-cloud layer between 400 m and 750–800 m, in correspondence with the negative temperature anomaly. This anomaly dipole confirms what we found in Figure 7b,d and can be due to dry and cold air being advected in the sub-cloud layer from upper layers by rain.

10 minutes after t_{min}, the mixing ratio displays patches that appear as a region with almost zero anomalies surrounded by an area of negative anomalies that grow to occupy the entire sub-cloud layer at 20 minutes from t_{min}. In correspondence with these patches, positive anomalies of vertical velocity are present, and at 30 min from t_{min} the wind field anomaly also reveals a dipole structure of updrafts and downdrafts exceeding $\pm\,0.3\,m\cdot s^{-1}$. This weaker dipole structure is connected with new convection and associated with weaker precipitation (see the radar reflectivity at 40 min from t_{min}). We do not see the same recovery in temperature after t_{min}, and the negative anomaly seems to persist in the sub-cloud layer up to 40 min from t_{min}. Dipole structures in vertical velocity anomalies are also visible from 1 hour to 20 min before the cold-pool feature, in a symmetrical time distance that could depend on the typical circular shape of cold pools spreading around precipitation. They are also associated with positive patches of humidity and with smaller precipitation events (see Figure 9c,d,f) between -60 and -20 min from t_{max}). Because we do not know the direction of movement of the cloud field and in which direction the ship is approaching the cold pool, we can only hypothesize that these features are due to new convective events activated by the cold pool. If the presence of the new convection can be interpreted as an indication of the edge of the cold pool, as happens in simulations in Tompkins (2001),

we can extrapolate a mean cold-pool size by multiplying the mean sub-cloud layer wind speed (Figure 4) for the time distance of the new convective event. The first positive updrafts are visible at 10 min from t_{min}. Hence, the mean expected radius for the cold pools analyzed should be around 6 km, a value slightly smaller than the mean cold-pool radius of 8 km but entirely in the range of variability of the distribution between 5 and 10 km obtained in Tompkins (2001).

The patterns of vertical wind-speed anomaly and mixing-ratio anomaly in the sub-cloud layer from slightly before t_{min} to 30 min after t_{min} strongly resemble qualitatively the composites of mean cold-pool water vapor perturbations of fig. 11 of Tompkins (2001). We do not have direct measurements of precipitation evaporation, but we can speculate from indirect observations. We expect that precipitation advects cold and dry air in the sub-cloud layer, of which we have evidence around t_{min}. The precipitation and the virga are visible in the radar before and after t_{min}, respectively. Their evaporation reinforces the cold anomaly in temperature and attenuates the dry anomaly in water vapor in the center of the sub-cloud layer at 500 m elevation. Moreover, they seem to break the positive moisture anomaly at t_{min}, as suggested by Langhans and Romps (2015). The slight positive anomaly of mixing ratio that emerges 10 minutes after t_{min} correlates with the positive anomaly in the vertical wind and seems to originate from the sea surface. As suggested by Langhans and Romps (2015), we believe these moisture patches existed in the boundary layer before (we saw them under the updraft region) and get undercut and displaced by the downdraft and then reinforced by the surface heat fluxes induced by the flow. Unfortunately, in our observations, the most apparent evidence of new convection is the onset of positive updrafts at a 20-minute time distance from the cold pool, more than from an evident moisture ring. We detect a moist layer that appears as a region with almost zero anomalies surrounded by an area of negative anomaly. As in Touzé-Peiffer et al. (2022), this patch is connected to the sea surface, probably mostly fed by surface evaporation due to the surface fluxes strengthened by the cold pool (Gentine et al., 2016). However, we have no evidence of positive moisture rings of 1–2 $g\cdot kg^{-1}$ near the edges of the cold pool, as suggested by Tompkins (2001).

6 | CONGESTUS PRECIPITATION AND ORGANIZATION: A CASE STUDY

Recently, much research has focused on understanding the role of cold pools in organizing cloud mesoscale patterns. Alinaghi et al. (2025) found that cold pools occur

more often in stronger geostrophic wind conditions and weaker significant subsidence and are synchronized with the diurnal cycle of solar radiation. Using an LES, Dauhut *et al.* (2023) found that cold pools and cloudy updrafts along large arcs can shape flower clouds. Vogel *et al.* (2021) demonstrated that most of the cold pools detected at the BCO site belong to the cloud patterns of gravel, followed by fish and flowers.

On February 12, 2020, the ship first sampled some small shallow clouds and then an organized group of congestus clouds (see Figure 10 and supplementary video S6); the ship was moving southward from a location east of Barbados in the circle area of the HALO Aircraft operations (Stevens *et al.*, 2021), crossing from 13.6°N, 57.2°W to 12.8°N, 52.7°W. Here, we would like to investigate the observed changes in the cloud and sub-cloud layer caused by the congestus clouds in relation to the cloud mesoscale organization as seen from satellite and ERA5 fields of vertical velocity, wind, and specific humidity. The first precipitation was recorded right before 1200 UTC, and from around 1500–1800 UTC we observed a series of precipitating events. These events can be seen in the peaks in liquid water path, showing saturating values around 1000 g · m^{-2} indicative of precipitation, and in the radar reflectivity profiles reaching the sea surface (Figure 10b). The liquid water path time series indicates that, from 1100 UTC until the onset of rain at 1500 UTC, the ship crosses a cloudy area with LWP values smaller than 100 g · m^{-2}, characterized by a constant surface relative humidity and temperature (Figure 10e,f). At 1500 UTC, we observed an abrupt change in the local conditions caused by precipitation and the associated cold pool. There are strong dry anomalies in water-vapor mixing ratio in the sub-cloud layer between 700 and 250 m, in combination with a substantial decrease of around 2 K in surface air temperature and a local increase in surface relative humidity, indicating the possibility of advection of cold, dry air from the upper layers associated with the precipitation event around 1530 UTC. All these signatures match perfectly the variability of conditions in the presence of cold pools that we detailed before. The positive anomaly in surface relative humidity reflects what Touzé-Peiffer *et al.* (2022) found. Similarly, less marked signatures are present for successive rain showers at 1600, 1640, and 1700 UTC. The satellite-based cloud-pattern classification by Chatterjee *et al.* (2024) (see supplementary material (S5) for more information about the satellite-based cloud classes) assigns class 5 to all the images collected before 1500 UTC and class 2 to all the images after 1500 UTC. Class 5, with integrated water vapor ranging from 30–32 kg · m^{-2} and low mean cloud cover of 27%, is the one with the lowest cloud fraction (Chatterjee *et al.*, 2024). Class 2, present from 1500 UTC onwards, shows an almost double cloud

cover, of 43%, and comprises more organized and optically thick shallow clouds (Chatterjee *et al.*, 2023).

We looked at the organization during the entire duration of the transition, from 1400 to 1800 UTC (Figure 11). ERA5 vertical velocity fields show that, while at the LCL the vertical velocity is always around zero, at 2000 m (cloud-top height) and 500 hPa the vertical velocity fields over the ship position change during the case study; subsidence of around −0.2 m · s^{-1} is reversed after 1500 UTC, displaying upward vertical velocities of +0.2 m · s^{-1} until 1800 UTC. At 2000 m, instead, a strong upward vertical velocity of 0.4 m · s^{-1} after 1500 UTC is reduced, and from 1700 UTC onwards it becomes negative up to −0.2 m · s^{-1}. Observations and ERA5 thus show that at 1500 UTC a substantial change in the local, as well as mesoscale, environmental conditions is taking place, supported also by a change in the satellite-based cloud-pattern classification. We clearly cannot prove any causality between the changes observed in ERA5 and those at the local scale. We hypothesize that, from 1500 UTC onwards, the ship is located in a moist SMOC object (George *et al.*, 2023), identifiable as the vertical velocity circular pattern we see at 1400 and 1500 UTC at 2000 m. Radiosondes (Figure 8b) show that congestus clouds before precipitating are moister than clear-sky conditions, so it is plausible to expect moister air compared with the mean state. At the same time, the positive vertical velocity at 2000 m could be, as in LES simulations from Narenpitak *et al.* (2021), helping the deepening of the boundary layer between 1400 and 1600 UTC and fostering the convergence of moisture. However, when precipitation sets in after 1500 UTC, vertical velocity at cloud top diminishes and then turns negative, probably also pushing a different cloud-pattern organization, as detected by the satellite classification method.

Two radiosondes were launched, one before and one after the cold-pool occurrence, to monitor possible changes in atmospheric conditions induced by the cold pool. We compare the profiles of equivalent potential temperature and specific humidity launched at 1415 and 1855 UTC, when cold-pool features are less pronounced. (Figure 12a,e). Generally, the profiles at 1855 UTC are drier and cooler at almost all heights compared with those at 1415 UTC. However, a striking difference between the two time stamps is given by the presence at cloud top (2000 m) of extremely dry and cool air, showing values of specific humidity around 2–3 g · kg^{-1} and values of θ_q almost 20 K smaller than the rest of the profile. We hypothesize that this dry and cold air mass is advected by precipitation in the cloud layer (in agreement with Figure 8). This is not just a transient feature: it persists for more than one hour after the cold pool is extinguished, potentially contributing to a new mesoscale cloud organization that the cold pool induced. The vertical velocity and horizontal
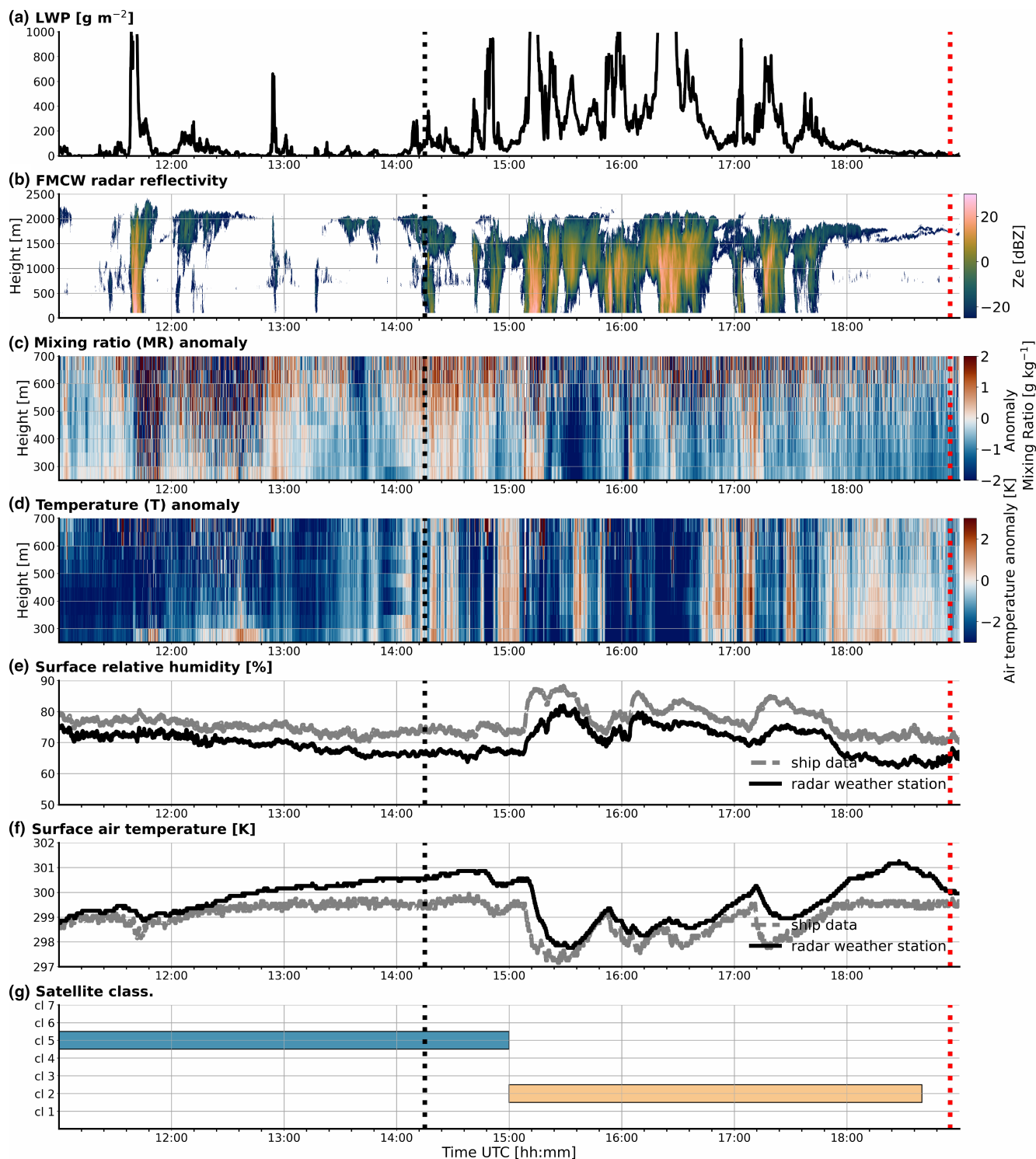
FIGURE 10 (a) Liquid water path, (b) FMCW radar reflectivity, (c) anomaly in water-vapor mixing ratio, (d) temperature anomaly, (e) surface relative humidity, and (f) surface air temperature and cloud-pattern classification from Chatterjee *et al.* (2024), occurring along the track of *RV MSM* (see also Video S6 in the Supporting Information). [Colour figure can be viewed at wileyonlinelibrary.com]

wind direction at 2000 and 3000 m (Figure 12b,f), the specific humidity (Figure 12c,g), and the equivalent potential temperature (Figure 12d,h) at the same elevations from ERA5 show the local circulation at 1900 UTC. Over the

ship position, the subsidence and the vertical velocity seem to advect towards the cloud-top height some dry air masses showing values of q and θ_e similar to those observed in the radiosoundings.
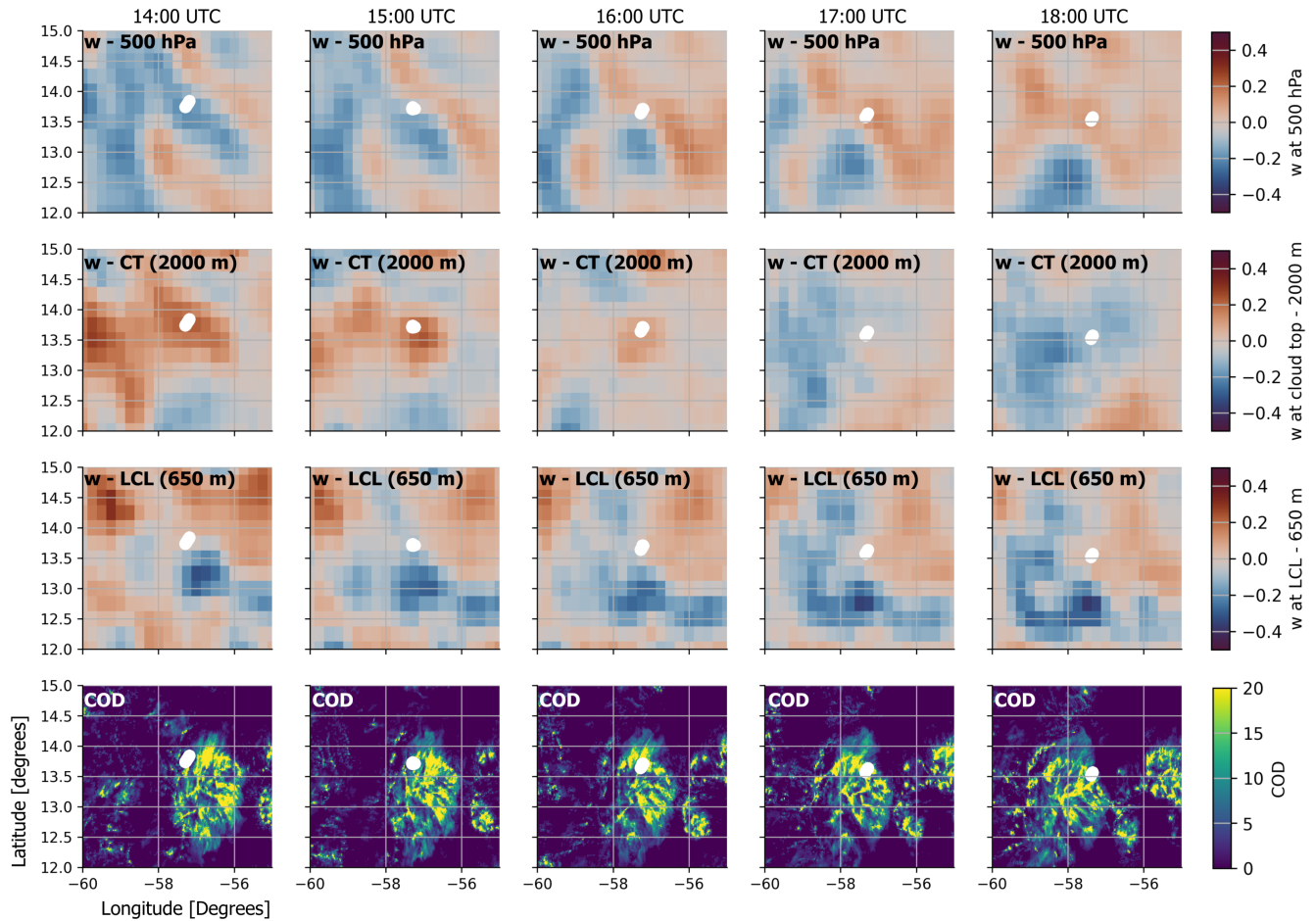
FIGURE 11 Vertical velocity from ERA5 at 500 hPa (first row), cloud-top height of 2000 m (second row), and LCL at 650 m (third row). Cloud optical thickness (COD) from satellite at every hour from 1400 to 1800 UTC. [Colour figure can be viewed at wileyonlinelibrary.com]

Observations seem to suggest that, as well as the 2000 m vertical velocity fostering convective activity, precipitation can also impact the vertical velocity field and induce a downward motion that seems to be proven by ERA5 data. However, we sincerely invite the modeling community to run LES simulations for this case study to verify and test our preliminary hypothesis on the links between congestus precipitation and changes in the vertical velocity field.

7 | CONCLUSIONS AND OUTLOOK

This work makes use of the synergy of ship-based remote-sensing profiling observations obtained aboard the *RV Maria S. Merian* during the EUREC⁴A field study that took place in the trade-wind-driven Tropical Atlantic in January and February 2020. As opposed to previous studies, here we analyze the shallow convection regime and how it affects the marine boundary-layer thermodynamic and dynamic structure in a statistical rather than a case-study based approach. Co-located observations

from FMCW cloud radar, ARTHUS Raman lidar, and two Doppler lidars focused on describing the cloud life cycle from formation to precipitation and its impacts on the marine boundary layer. The trade-wind region has been studied for a long time in dedicated modeling and observational studies like RICO (Rauber *et al.*, 2007). During the EUREC⁴A campaign, we used a unique set of instruments capable of achieving an unprecedented temporal and spatial resolution in sampling of the marine boundary layer, a critical region for cloud and precipitation development. Such observations are also essential for reducing errors in satellite observations of marine boundary-layer warm clouds in terms of resolution, detection limits, and near-surface blind zones (Lamer *et al.*, 2020). This analysis also represents a valuable benchmark dataset for future model evaluation.

Clouds and precipitation are classified as *shallow* or *congestus* based on their geometrical thickness. We first analyzed the daily cycle of shallow and congestus clouds to understand how clouds evolve during the day and in which thermodynamical conditions. Shallow clouds show very little variability during the whole day, instead
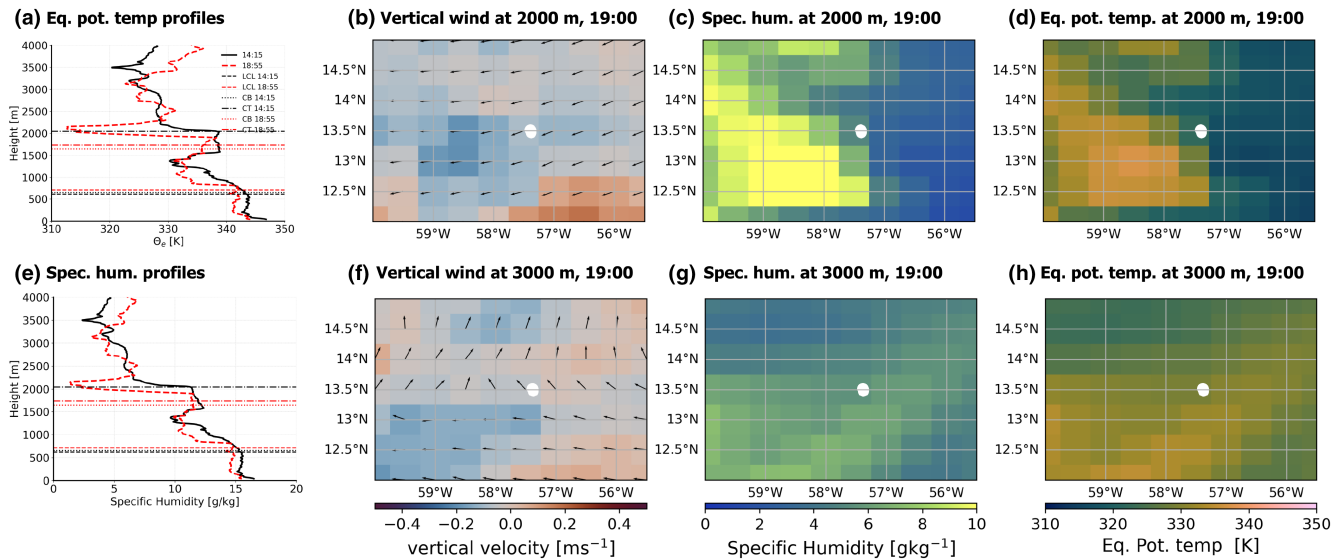
FIGURE 12 (a) Equivalent potential temperature θ_e profiles from the radiosondes launched at 1415 and 1855 UTC. (b) Vertical velocity (color shaded) and wind direction (black vectors) at 1900 UTC at cloud-base height (2000 m from ERA5. (c) Specific humidity at 1900 UTC at cloud-base height (2000 m) from ERA5. (d) Equivalent potential temperatue θ_e at cloud-base height (2000 m) from ERA5. (e) Specific humidity profiles from the radiosondes launched at 1415 and 1855 UTC. (f) Same as in (b) but at 3000 m. (g) Same as in (c) but at 3000 m. (h) Same as in (d) but at 3000 m. [Colour figure can be viewed at wileyonlinelibrary.com]

of maximizing during daytime as in Vial *et al.* (2023), while congestus show more substantial variations in cloud amount and cloud-top height, with some peaks of occurrence in the afternoon and evening, in agreement with the maximization at night shown in Vial *et al.* (2023). These results are in contrast with the clear minima in cloud cover reported by Vial *et al.* (2019). For rainy congestus clouds, we observe the highest values of rainy hydrometeor cloud fraction between 1200 and 2200 UTC, when the relative occurrence of rainy congestus clouds is minimum.

We then investigated how shallow and congestus clouds evolve when liquid water increases and how thermodynamic and dynamic fields change in their presence. Shallow non-precipitating clouds (Figure 13a) are characterized by a clear adiabatic growth when LWP values are below $100 \, g \cdot m^{-2}$. They are often initiated in moist ($+1 \, g \cdot kg^{-1}$) patches of humidity in the sub-cloud layer, sometimes induced by the sea surface, and form with ascending currents ($+0.1 \, m \cdot s^{-1}$) of air from the sub-cloud layer that are moister compared with clear-sky conditions. Clouds form at the LCL, with a release of latent heat that causes a local $+2 \, K$ increase in the potential temperature, and show minimal radar reflectivity values. Positive cloud radar Doppler skewness values indicate for these clouds the embryonic presence of tiny drizzle droplets.

In our observations, shallow clouds appear as a precursor stage of congestus clouds (Figure 13b,c), which do not show evident anomalies in vertical velocity before precipitating. The dynamic contribution to cloud formation happens in the initial development phase of the shallow

cloud. Then, other processes, like microphysical and thermodynamic processes, support further cloud development stages in the congestus phase. Condensation, for example, releases heat to the environment, and collision coalescence generates the droplets that, once they have reached a given size, become unstable and start to precipitate. As in Lamer *et al.* (2015), we identified a threshold value of $-20 \, dBZ$ to discriminate between non-precipitating cumuli and cumuli with particle sedimentation. We located the transition from the adiabatic regime to a profile with larger reflectivities aloft between 1500 and 2000 m. In that height range, collision–coalescence between cloud droplets ($-20 \, dBZ$ radar reflectivity) and larger drizzle drops ($-5 \, dBZ$) leads to the initiation of precipitation. Also, in congestus clouds, the air contains more moisture than the clear-sky air. However, this decreases with elevation due to condensation slightly below the LCL.

We then investigated the impact of virga and precipitation on the sub-cloud layer. For shallow clouds (Figure 13e), virga evaporation contributes mainly to cooling ($-0.5 \, K$) and moistening ($+1 \, g \cdot kg^{-1}$) the sub-cloud layer in the area extending 200–300 m below the cloud base. In congestus cloud conditions (Figure 13d), virga is more extended in the sub-cloud layer, and, while falling, advects dry and cold air from the upper layers, causing a cooling anomaly of $-0.5 \, g \cdot kg^{-1}$ in the sub-cloud layer. In congestus rainy conditions, air up to 3 K cooler and $2 \, g \cdot kg^{-1}$ drier than non-rainy congestus conditions is advected in the cloud layer: this is documented using a statistic of radiosonde profiles launched in precipitating
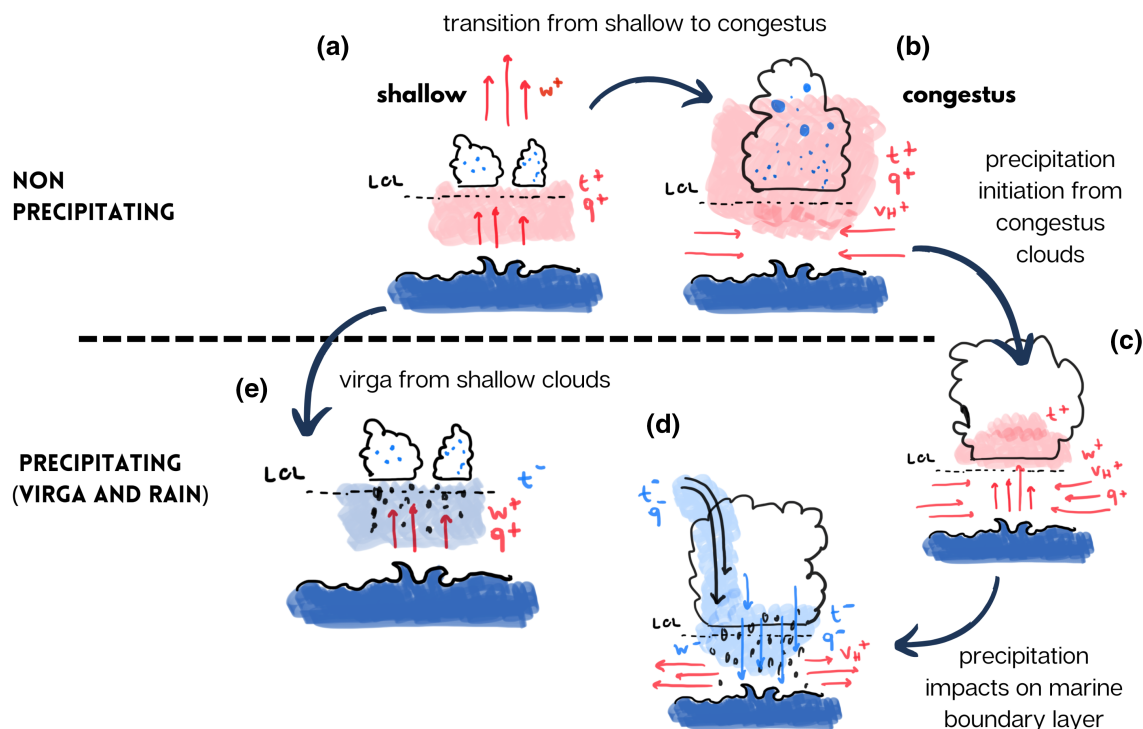
FIGURE 13 Schematic representation of the main processes described in this work. Color-shaded areas represent temperature anomalies (t^+ in red, t^- in blue), while q anomalies are indicated as q^+ and q^-. Positive vertical and horizontal wind anomalies are reported with red arrows. Shallow clouds form in the presence of updrafts and warmer moisture patches. They can evolve further in congestus clouds when updrafts extend above the cloud base or vanish, eventually producing virga, which typically moistens and cools the sub-cloud layer. Congestus clouds develop in warmer and more humid environments compared with clear-sky conditions, and typically contain larger droplets of different sizes. This variability, when coupled with favorable environmental conditions, can produce rain, which impacts the sub-cloud layer strongly, with dry and cold temperature anomalies caused by the advection of air from the upper layers. [Colour figure can be viewed at wileyonlinelibrary.com]

conditions, as well as by compiling a statistic of cold-pool cases. The downward motion of dry cold air is in agreement with previous modeling and observational studies (Langhans & Romps, 2015; Tompkins, 2001; Zuidema et al., 2011).

From the cold-pool statistics, we also found that water-vapor mixing ratio patches form under the cloud's convective core and decrease dramatically after the onset of the cold pool when they are undercut by precipitation. They then recover after 20 min, pushed by surface fluxes as predicted by Langhans and Romps (2015). This is qualitatively similar to the description in Tompkins (2001). The same behavior is true for vertical wind speeds. However, we do not observe a temperature recovery to the pre-cold-pool value in the hour after the cold-pool event.

Finally, we characterized a cold-pool case study and investigated the variability of the vertical velocity, horizontal wind direction, and absolute humidity at cloud top in ERA5 data. We found that the vertical velocity over the congestus clouds is positive until 1500 UTC before precipitation starts and can thus potentially help the deepening of the boundary layer, as shown in Narenpitak

et al. (2021). After the onset of precipitation from 1500 UTC onwards, we see a reduction in vertical velocity at cloud top, which might be connected to the precipitation and the induced cold pool. The negative vertical velocity at cloud top observed from 1800 to 1900 UTC agrees with the presence of dry cold air observed at the same height in the radiosonde launched at 1900 UTC. This evidence documents the duration of the perturbations induced by the cold-pool case study for at least one hour after the end of the cold pool. Open questions remain: is it the precipitation that induces the reduction in vertical velocity at cloud top, or vice versa, does the mesoscale vertical velocity field drive the onset of precipitation in the congestus clouds? Observations cannot answer this question, and an LES simulation of this case study would help us to understand the causal relationship between the observed behaviors.

The statistical analysis presented in this work stands as a benchmark for model evaluation of all the physical, dynamic, and thermodynamic processes we highlighted. We are eager to compare these results with model runs conducted over the *RV Maria S. Merian* ship track to evaluate process representations in models quantitatively.

Moreover, further research investigating virga properties is under development. Drop-size distributions of virga and rain are being retrieved to be used as a basis for developing a rain evaporation rate retrieval, a crucial parameter for understanding the role of precipitation in moistening the sub-cloud layer.

Various research (Becker *et al.*, 2024) has focused on the difficulty of all Global CLimate Model–Next Generation of Earth Modeling Systems (GCM-NEXTGEMS) models in representing the aggregation of convective precipitating systems correctly. Moreover, mesoscale organization is crucial for the variation of tropical daily accumulated precipitation extremes (Bao *et al.*, 2024; Wolding *et al.*, 2024). Many authors believe that such difficulties are due to the representation of convection triggering and boundary-layer moistening. Providing a benchmark for improving model behavior through bias evaluation is a first step towards understanding and describing these processes better.

CONFLICT OF INTEREST STATEMENT

The authors declare no conflicts of interest.

DATA AVAILABILITY STATEMENT

The data that support the findings of this study are openly available in "Liquid water path and Doppler radar moments observations from the 94 GHz FMCW-band radar deployed on *R/V Maria S. Merian* during EUREC^{4}A campaign—V2" at https://doi.org/10.25326 /235 (Acquistapace et al. 2021). The most recent version of the liquid water path data is available in "Ground- and ship-based microwave radiometer measurements during EUREC^{4}A" at https://doi.org/10.25326/454#v2.0 (Schnitt et al. 2023). Satellite data (training data and deep-learning software and pre-trained weights) are available in (2024), https://doi.org/10.1029/2024GL108889 and (Chatterjee et al. 2023), https://zenodo.org/records/8352614. Radiosounding data are available in "Radiosonde measurements from the EUREC^{4}A field campaign (v3.0.0)" at https://doi.org/10.25326/137 (Stephan et al. 2020). The ARTHUS Raman lidar and Doppler lidar data collected during the EUREC4A Campaign are available at https://doi.org/10.5281/zenodo.16992362.

ENDNOTE

[1] https://unidata.github.io/MetPy/latest/index.html, last accessed July 21, 2025.

ORCID

Claudia Acquistapace ⓘ https://orcid.org/0000-0002 -1144-4753
Sabrina Schnitt ⓘ https://orcid.org/0000-0002-3949-770X
Nils Risse ⓘ https://orcid.org/0000-0002-7267-9353
Diego Lange ⓘ https://orcid.org/0000-0002-1185-7152
Dwaipayan Chatterjee ⓘ https://orcid.org/0000-0001 -8757-9884

REFERENCES

Acquistapace, C., Coulter, R., Crewell, S., Garcia-Benadi, A., Gierens, R., Labbri, G. et al. (2022a) Eurec^{4}a's *Maria S. Merian* ship-based cloud and micro rain radar observations of clouds and precipitation. *Earth System Science Data*, 14(1), 33–55. Available from: https://doi.org/10.5194/essd-14-33-2022

Acquistapace, C., Löhnert, U., Maahn, M. & Kollias, P. (2019) A new criterion to improve operational drizzle detection with ground-based remote sensing. *Journal of Atmospheric and Oceanic Technology*, 36, 781–801. Available from: https://doi.org /10.1175/JTECH-D-18-0158.1

Acquistapace, C., Meroni, A.N., Labbri, G., Lange, D., Späth, F., Abbas, S. et al. (2022b) Fast atmospheric response to a cold oceanic mesoscale patch in the north-western tropical atlantic. *Journal of Geophysical Research: Atmospheres*, 127(21), e2022JD036799. Available from: https://doi.org /2022JD036799

Acquistapace, C., Schween, J.H., Risse, N., Haseneder-Lind, R., Klocke, D., Röttenbacher, J. et al. (2021) Liquid water path and Doppler radar moments observations from the 94 GHz FMCW-band radar deployed on R/V Maria S. Merian during EUREC4A campaign - V2.[dataset]. Aeris. https://doi.org/10.25326/235

Albright, A.L., Stevens, B., Bony, S. & Vogel, R. (2023) A new conceptual picture of the trade wind transition layer. *Journal of the Atmospheric Sciences*, 80(6), 1547–1563. Available from: https://doi.org/10.1175/JAS-D-22-0184.1

Alinaghi, P., Siebesma, A.P., Jansson, F., Janssens, M. & Glassmeier, F. (2025) External drivers and mesoscale self-organization of shallow cold pools in the trade-wind regime. *Journal of Advances in Modeling Earth Systems*, 17(1), e2024MS004540. Available from: https://doi.org/10.1029/2024MS004540

Bao, J., Stevens, B., Kluft, L. & Muller, C. (2024) Intensification of daily tropical precipitation extremes from more organized convection. *Science Advances*, 10(8), eadj6801. Available from: https://doi.org/10.1126/sciadv.adj6801

Becker, T., Takasuka, D. & Bao, J. (2024) Characteristics of precipitating convection and moisture-convection relationships in global km-scale simulations. *EGU General Assembly*, 17683, EGU24–EGU17683. Available from: https://doi.org/10.5194/egusphere-egu24-17683

Beheng, K.D. (2010) Rainfall:the state of science. In *The evolution of raindrop spectra: a review of microphysical essentials*, pp. 29–48, American Geophysical Union (AGU), Washington, D.C. https://agupubs.onlinelibrary.wiley.com/doi/book/10.1029/GM191

Behrendt, A., Wulfmeyer, V., Senff, C., Muppa, S.K., Späth, F., Lange, D. et al. (2020) Observation of sensible and latent heat flux profiles with lidar. *Atmospheric Measurement Techniques*, 13(6), 3221–3233. Available from: https://doi.org/10.5194/amt-13-3221-2020

Bony, S. & Dufresne, J.L. (2005) Marine boundary layer clouds at the heart of tropical cloud feedback uncertainties in climate models. *Geophysical Research Letters*, 32(20), 2005GL023851. Available from: https://doi.org/10.1029/2005GL023851

Bony, S., Dufresne, J., Treut, H.L., Morcrette, J.J. & Senior, C.A. (2004) On dynamic and thermodynamic components of cloud changes. *Climate Dynamics*, 22, 71–86. Available from: https://api.semanticscholar.org/CorpusID:56077074

Bony, S., Schulz, H., Vial, J. & Stevens, B. (2020) Sugar, gravel, fish, and flowers: dependence of mesoscale patterns of trade-wind clouds on environmental conditions. *Geophysical Research Letters*, 47(7), e2019GL085988. Available from: https://doi.org/10.1029/2019GL085988

Bony, S., Stevens, B., Ament, F., Bigorre, S., Chazette, P., Crewell, S. et al. (2017) EUREC4A: a field campaign to elucidate the couplings between clouds, convection and circulation. *Surveys in Geophysics*, 38(6), 1529–1568. Available from: https://doi.org/10.1007/s10712-017-9428-0

Bretherton, C.S. & Blossey, P.N. (2017) Understanding mesoscale aggregation of shallow cumulus convection using large-eddy simulation. *Journal of Advances in Modeling Earth Systems*, 9(8), 2798–2821. Available from: https://doi.org/10.1002/2017MS000981

Bretherton, C.S., Blossey, P.N. & Khairoutdinov, M. (2005) An energy-balance analysis of deep convective self-aggregation above uniform sst. *Journal of the Atmospheric Sciences*, 62(12), 4273–4292. Available from: https://doi.org/10.1175/JAS3614.1

Chatterjee, D., Acquistapace, C., Deneke, H. & Crewell, S. (2023) Understanding cloud systems' structure and organization using a machine's self-learning approach. *Artificial Intelligence for the Earth Systems*, 2(4), e220096. Available from: https://doi.org/10.1175/AIES-D-22-0096.1

Chatterjee, D., Schnitt, S., Bigalke, P., Acquistapace, C. & Crewell, S. (2024) Capturing the diversity of mesoscale trade wind cumuli using complementary approaches from self-supervised deep learning. *Geophysical Research Letters*, 51(12), e2024GL108889. Available from: https://doi.org/10.1029/2024GL108889

Chatterjee,D., Schnitt, S., Bigalke, P., Acquistapace, C., & Crewell, S. (2023) Codes and pretrained weights for the study 'Capturing the diversity of mesoscale trade wind cumuli using complementary approaches from self-supervised deep learning'. https://doi.org/10.5281/zenodo.8352614

Chen, X., Dias, J., Wolding, B., Pincus, R., DeMott, C., Wick, G. et al. (2023) Ubiquitous sea surface temperature anomalies increase spatial heterogeneity of trade wind cloudiness on daily time scale. *Journal of the Atmospheric Sciences*, 80(12), 2969–2987. Available from: https://doi.org/10.1175/JAS-D-23-0075.1

Crameri, F., Shephard, G.E. & Heron, P.J. (2020) The misuse of colour in science communication. *Nature Communications*, 11(1), 5444. Available from: https://doi.org/10.1038/s41467-020-19160-7

Dauhut, T., Couvreux, F., Bouniol, D., Beucher, F., Volkmer, L., Pörtge, V. et al. (2023) Flower trade-wind clouds are shallow mesoscale convective systems. *Quarterly Journal of the Royal Meteorological Society*, 149(750), 325–347. Available from: https://doi.org/10.1002/qj.4409

Denby, L. (2020) Discovering the importance of mesoscale cloud organization through unsupervised classification. *Geophysical Research Letters*, 47(1), e2019GL085190. Available from: https://doi.org/10.1029/2019GL085190

Denby, L. (2023) Charting the realms of mesoscale cloud organisation using unsupervised learning.

Feingold, G., Cotton, W., Kreidenweis, S. & Davis, J. (1999) The impact of giant cloud condensation nuclei on drizzle formation in stratocumulus: implications for cloud radiative properties. *Journal of the Atmospheric Sciences*, 56(24), 4100–4117. Available from: https://doi.org/10.1175/1520-0469(1999)056<4100:TIOGCC>2.0.CO;2

Gentine, P., Garelli, A., Park, S.B., Nie, J., Torri, G. & Kuang, Z. (2016) Role of surface heat fluxes underneath cold pools. *Geophysical Research Letters*, 43(2), 874–883. Available from: https://doi.org/10.1002/2015GL067262

George, G., Stevens, B., Bony, S., Vogel, R. & Naumann, A.C. (2023) Widespread shallow mesoscale circulations observed in the trades. *Nature Geoscience*, 16, 584–589. Available from: https://doi.org/10.1038/s41561-023-01215-1

Ghate, V.P., Miller, M.A. & DiPretore, L. (2011) Vertical velocity structure of marine boundary layer trade wind cumulus clouds. *Journal of Geophysical Research*, 116(D16), D16206. Available from: https://doi.org/10.1029/2010JD015344

Grabowski, W.W. & Wang, L.P. (2013) Growth of cloud droplets in a turbulent environment. *Annual Review of Fluid Mechanics*, 45(1), 293–324. Available from: https://doi.org/10.1146/annurev-fluid-011212-140750

Grandpeix, J.Y. & Lafore, J.P. (2010) A density current parameterization coupled with emanuel's convection scheme. Part i: the models. *Journal of the Atmospheric Sciences*, 67(4), 881–897. Available from: https://doi.org/10.1175/2009JAS3044.1

Hersbach, H., Bell, B., Berrisford, P., Hirahara, S., Horányi, A., Muñoz-Sabater, J. et al. (2020) The era5 global reanalysis. *Quarterly Journal of the Royal Meteorological Society*, 146(730), 1999–2049. Available from: https://doi.org/10.1002/qj.3803

Holland, J. & Rasmusson, E. (1973) Measurements of the atmospheric mass, energy, and momentum budgets over a 500-kilometer square of tropical ocean. *Monthly Weather Review*, 101(1), 44–55. Available from: https://doi.org/10.1175/1520-0493(1973)101<0044:MOTAME>2.3.CO;2

Jacob, M., Kollias, P., Ament, F., Schemann, V. & Crewell, S. (2020) Multilayer cloud conditions in trade wind shallow cumulus – confronting two icon model derivatives with airborne observations. *Geoscientific Model Development*, 13(11), 5757–5777. Available from: https://doi.org/10.5194/gmd-13-5757-2020

Janssens, M., De Arellano, J.V.G., Van Heerwaarden, C.C., De Roode, S.R., Siebesma, A.P. & Glassmeier, F. (2023) Nonprecipitating shallow cumulus convection is intrinsically unstable to length scale growth. *Journal of the Atmospheric Sciences*, 80(3), 849–870. Available from: https://doi.org/10.1175/JAS-D-22-0111.1

Janssens, M., George, G., Schulz, H., Couvreux, F. & Bouniol, D. (2024) Shallow convective heating in weak temperature gradient balance explains mesoscale vertical motions in the trades. *Journal of Geophysical Research: Atmospheres*, 129(18), e2024JD041417. Available from: https://doi.org/10.1029/2024JD041417

Janssens, M., Vilà-Guerau de Arellano, J., Scheffer, M., Antonissen, C., Siebesma, A.P. & Glassmeier, F. (2021) Cloud patterns in the trades have four interpretable dimensions. *Geophysical Research Letters*, 48(5), e2020GL091001. Available from: https://doi.org/10.1029/2020GL091001

Kalesse-Los, H., Kötsche, A., Foth, A., Röttenbacher, J., Vogl, T. & Witthuhn, J. (2023) The virga-sniffer – a new tool to identify precipitation evaporation using ground-based remote-sensing observations. *Atmospheric Measurement Techniques*, 16(6), 1683–1704. Available from: https://doi.org/10.5194/amt-16-1683-2023

Kollias, P. & Albrecht, B. (2010) Vertical velocity statistics in fair-weather cumuli at the arm twp nauru climate research facility. *Journal of Climate*, 23(24), 6590–6604. Available from: https://doi.org/10.1175/2010JCLI3449.1

Kollias, P., Rémillard, J., Luke, E. & Szyrmer, W. (2011) Cloud radar doppler spectra in drizzling stratiform clouds: 1. Forward modeling and remote sensing applications. *Journal of Geophysical Research: Atmospheres*, 116(D13): 0148–0227. Available from: https://doi.org/10.1029/2010JD015237

Konow, H., Ewald, F., George, G., Jacob, M., Klingebiel, M., Kölling, T. et al. (2021) Eurec⁴a's. *HALO. Earth System Science Data*, 13(12), 5545–5563. Available from: https://doi.org/10.5194/essd-13-5545-2021

Lamer, K., Kollias, P. & Nuijens, L. (2015) Observations of the variability of shallow trade wind cumulus cloudiness and mass flux. *Journal of Geophysical Research: Atmospheres*, 120(12), 6161–6178. Available from: https://doi.org/10.1002/2014JD022950

Lamer, K., Kollias, P., Battaglia, A. & Preval, S. (2020) Mind the gap – part 1: accurately locating warm marine boundary layer clouds and precipitation using spaceborne radars. *Atmospheric Measurement Techniques*, 13(5), 2363–2379. Available from: https://doi.org/10.5194/amt-13-2363-2020

Lange, D., Behrendt, A. & Wulfmeyer, V. (2019) Compact operational tropospheric water vapor and temperature raman lidar with turbulence resolution. *Geophysical Research Letters*, 46(24), 14844–14853. Available from: https://doi.org/10.1029/2019GL085774

Langhans, W. & Romps, D.M. (2015) The origin of water vapor rings in tropical oceanic cold pools. *Geophysical Research Letters*, 42(18), 7825–7834. Available from: https://doi.org/10.1002/2015GL065623

Lau, K.M. & Wu, H.T. (2003) Warm rain processes over tropical oceans and climate implications. *Geophysical Research Letters*, 30(24), 2003GL018567. Available from: https://doi.org/10.1029/2003GL018567

Li, Y. & Carbone, R.E. (2012) Excitation of rainfall over the tropical western pacific. *Journal of the Atmospheric Sciences*, 69(10), 2983–2994. Available from: https://doi.org/10.1175/JAS-D-11-0245.1

Luke, E.P. & Kollias, P. (2013) Separating cloud and drizzle radar moments during precipitation onset using Doppler spectra. *Journal of Atmospheric and Oceanic Technology*, 30(8), 1656–1671. Available from: https://doi.org/10.1175/JTECH-D-11-00195.1

Narenpitak, P., Kazil, J., Yamaguchi, T., Quinn, P. & Feingold, G. (2021) From sugar to flowers: a transition of shallow cumulus organization during atomic. *Journal of Advances in Modeling Earth Systems*, 13(10), e2021MS002619. Available from: https://doi.org/10.1029/2021MS002619

Naumann, A.K., Stevens, B., Hohenegger, C. & Mellado, J.P. (2017) A conceptual model of a shallow circulation induced by prescribed low-level radiative cooling. *Journal of the Atmospheric Sciences*, 74(10), 3129–3144. Available from: https://doi.org/10.1175/JAS-D-17-0030.1

Nuijens, L., Stevens, B. & Siebesma, A.P. (2009) The environment of precipitating shallow cumulus convection. *Journal of the Atmospheric Sciences*, 66(7), 1962–1979. Available from: https://doi.org/10.1175/2008JAS2841.1

Nujens, L. & Siebesma, P. (2019) Boundary layer clouds and convection over subtropical oceans in our current and in a warmer climate. *Current Climate Change Reports*, 5, 80–94. Available from: https://doi.org/10.1007/s40641-019-00126-x

Pal, S.R., Steinbrecht, W. & Carswell, A.I. (1992) Automated method for lidar determination of cloud-base height and vertical extent. *Applied Optics*, 31(10), 1488–1494. Available from: https://doi.org/10.1364/AO.31.001488

Pearson, G., Davies, F. & Collier, C. (2009) An analysis of the performance of the UFAM pulsed Doppler lidar for observing the boundary layer. *Journal of Atmospheric and Oceanic Technology*, 26, 240–250. Available from: https://doi.org/10.1175/2008JTECHA1128.1

Radtke, J., Naumann, A.K., Hagen, M. & Ament, F. (2022) The relationship between precipitation and its spatial pattern in the trades observed during eurec4a. *Quarterly Journal of the Royal Meteorological Society*, 148(745), 1913–1928. Available from: https://doi.org/10.1002/qj.4284

Rasp, S., Schulz, H., Bony, S. & Stevens, B. (2020) Combining crowdsourcing and deep learning to explore the mesoscale Organization of Shallow Convection. *Bulletin of the American Meteorological Society*, 101(11), E1980–E1995. Available from: https://doi.org/10.1175/BAMS-D-19-0324.1

Rauber, R.M., Stevens, B., Ochs, H.T., Knight, C., Albrecht, B.A., Blyth, A.M. et al. (2007) Rain in shallow cumulus over the ocean: the RICO campaign. *Bulletin of the American Meteorological*

Society, 88(12), 1912–1928. Available from: https://doi.org/10.1175/BAMS-88-12-1912

Rochetin, N., Hohenegger, C., Touzé-Peiffer, L. & Villefranque, N. (2021) A physically based definition of convectively generated density currents: detection and characterization in convection-permitting simulations. *Journal of Advances in Modeling Earth Systems*, 13(7), e2020MS002402. Available from: https://doi.org/10.1029/2020MS002402

Romps, D.M. (2017) Exact expression for the lifting condensation level. *Journal of the Atmospheric Sciences*, 74(12), 3891–3900. Available from: https://doi.org/10.1175/JAS-D-17-0102.1

Savazzi, A.C.M., Nuijens, L., Sandu, I., George, G. & Bechtold, P. (2022) The representation of the trade winds in ecmwf forecasts and reanalyses during eurec[4]a. *Atmospheric Chemistry and Physics*, 22(19), 13049–13066. Available from: https://doi.org/10.5194/acp-22-13049-2022

Schmit, T.J., Gunshor, M.M., Menzel, W.P., Gurka, J.J., Li, J. & Bachmeier, A.S. (2005) Introducing the next-generation advanced baseline imager on goes-r. *Bulletin of the American Meteorological Society*, 86(8), 1079–1096. Available from: https://doi.org/10.1175/BAMS-86-8-1079

Schnitt, S., Foth, A., Kalesse-Los, H., Mech, M. & Acquistapace, C. (2023) Ground- and ship-based microwave radiometer measurements during EUREC4A. [dataset]. Aeris. https://doi.org/10.25326/454#v2.0

Schnitt, S., Foth, A., Kalesse-Los, H., Mech, M., Acquistapace, C., Jansen, F. et al. (2024) Ground- and ship-based microwave radiometer measurements during eurec[4]a. *Earth System Science Data*, 16(1), 681–700. Available from: https://doi.org/10.5194/essd-16-681-2024

Schulz, H. (2022) C[3]ontext: a common consensus on convective organization during the eurec[4]a experiment. *Earth System Science Data*, 14(3), 1233–1256. Available from: https://doi.org/10.5194/essd-14-1233-2022

Schulz, H., Eastman, R. & Stevens, B. (2021) Characterization and evolution of organized shallow convection in the downstream North Atlantic trades. *Journal of Geophysical Research: Atmospheres*, 126(17), e2021JD034575. Available from: https://doi.org/10.1029/2021JD034575

Seifert, A. & Heus, T. (2013) Large-eddy simulation of organized precipitating trade wind cumulus clouds. *Atmospheric Chemistry and Physics*, 13(11), 5631–5645. Available from: https://doi.org/10.5194/acp-13-5631-2013

Short, D.A. & Nakamura, K. (2000) Trmm radar observations of shallow precipitation over the tropical oceans. *Journal of Climate*, 13(23), 4107–4124. Available from: https://doi.org/10.1002/qj.4284

Siebesma, A.P., Bretherton, C.S., Brown, A., Chlond, A., Cuxart, J., Duynkerke, P.G. et al. (2003) A large eddy simulation intercomparison study of shallow cumulus convection. *Journal of the Atmospheric Sciences*, 60(10), 1201–1219. Available from: https://doi.org/10.1175/1520-0469(2003)60<1201:ALESIS>2.0.CO;2

Snodgrass, E.R., Girolamo, L.D. & Rauber, R.M. (2009) Precipitation characteristics of trade wind clouds during rico derived from radar, satellite, and aircraft measurements. *Journal of Applied Meteorology and Climatology*, 48(3), 464–483. Available from: https://doi.org/10.1175/2008JAMC1946.1

Späth, F., Behrendt, A., Brewer, W.A., Lange, D., Senff, C., Turner, D.D. et al. (2022) Simultaneous observations of surface layer profiles of humidity, temperature, and wind using scanning lidar instruments. *Journal of Geophysical Research: Atmospheres*, 127(5), e2021JD035697. Available from: https://doi.org/10.1029/2021JD035697

Stephan, C., Schnitt, S., Schulz, H. & Bellenger, H. (2020) Radiosonde measurements from the EUREC4A field campaign (v3.0.0). [dataset]. Aeris. https://doi.org/10.25326/137

Stephan, C.C., Schnitt, S., Schulz, H., Bellenger, H., de Szoeke, S.P., Acquistapace, C. et al. (2021) Ship- and island-based atmospheric soundings from the 2020 EUREC[4]a field campaign. *Earth System Science Data*, 13(2), 491–514. Available from: https://doi.org/10.5194/essd-13-491-2021

Stevens, B., Ackerman, A.S., Albrecht, B.A., Brown, A.R., Chlond, A., Cuxart, J. et al. (2001) Simulations of trade wind cumuli under a strong inversion. *Journal of the Atmospheric Sciences*, 58(14), 1870–1891. Available from: https://doi.org/10.1175/1520-0469(2001)058<1870:SOTWCU>2.0.CO;2

Stevens, B., Bony, S., Brogniez, H., Hentgen, L., Hohenegger, C., Kiemle, C. et al. (2020) Sugar, gravel, fish and flowers: mesoscale cloud patterns in the trade winds. *Quarterly Journal of the Royal Meteorological Society*, 146(726), 141–152. Available from: https://doi.org/10.1002/qj.3662

Stevens, B., Bony, S., Farrell, D., Ament, F., Blyth, A., Fairall, C. et al. (2021) Eurec[4]a. *Earth System Science Data Discussions*, 13, 1–78. Available from: https://doi.org/10.5194/essd-2021-18

Stevens, B., Farrell, D., Hirsch, L., Jansen, F., Nuijens, L., Serikov, I. et al. (2015) The Barbados cloud observatory: anchoring investigations of clouds and circulation on the edge of the ITCZ. *Bulletin of the American Meteorological Society*, 97(5), 787–801. Available from: https://doi.org/10.1175/BAMS-D-14-00247.1

Tompkins, A.M. (2001) Organization of tropical convection in low vertical wind shears: the role of cold pools. *Journal of the Atmospheric Sciences*, 58(13), 1650–1672. Available from: https://doi.org/10.1175/1520-0469(2001)058<1650:OOTCIL>2.0.CO;2

Touzé-Peiffer, L., Vogel, R. & Rochetin, N. (2022) Cold pools observed during eurec4a: detection and characterization from atmospheric soundings. *Journal of Applied Meteorology and Climatology*, 61(5), 593–610. Available from: https://doi.org/10.1175/JAMC-D-21-0048.1

van der Maaten, L. & Hinton, G. (2008) Visualizing data using t-sne. *Journal of Machine Learning Research*, 986, 2579–2605.

Vial, J., Albright, A.L., Vogel, R., Musat, I. & Bony, S. (2023) Cloud transition across the daily cycle illuminates model responses of trade cumuli to warming. *Proceedings of the National Academy of Sciences of the United States of America*, 120(8), e2209805120. Available from: https://doi.org/10.1073/pnas.2209805120

Vial, J., Dufresne, J. & Sandrine, B. (2013) On the interpretation of inter-model spread in cmip5 climate sensitivity estimates. *Clinical Dynamics*, 41, 3339–3362.

Vial, J., Vogel, R. & Schulz, H. (2021) On the daily cycle of mesoscale cloud organization in the winter trades. *Quarterly Journal of the Royal Meteorological Society*, 147(738), 2850–2873. Available from: https://doi.org/10.1002/qj.4103

Vial, J., Vogel, R., Bony, S., Stevens, B., Winker, D.M., Cai, X. et al. (2019) A new look at the daily cycle of trade wind cumuli. *Journal of Advances in Modeling Earth Systems*, 11(10), 3148–3166. Available from: https://doi.org/10.1029/2019MS001746

Vogel, R., Konow, H., Schulz, H. & Zuidema, P. (2021) A climatology of trade-wind cumulus cold pools and their link to mesoscale cloud organization. *Atmospheric Chemistry and Physics*, 21(21), 16609–16630. Available from: https://doi.org/10.5194/acp-21-16609-2021

Vogel, R., Nuijens, L. & Stevens, B. (2016) The role of precipitation and spatial organization in the response of trade-wind clouds to

warming. *Journal of Advances in Modeling Earth Systems*, 8(2), 843–862. Available from: https://doi.org/10.1002/2015MS000568

Walther, A. & Heidinger, A.K. (2012) Implementation of the daytime cloud optical and microphysical properties algorithm (dcomp) in patmos-x. *Journal of Applied Meteorology and Climatology*, 51(7), 1371–1390. Available from: https://doi.org/10.1175/JAMC-D-11-0108.1

Wang, H. & Feingold, G. (2009) Modeling mesoscale cellular structures and drizzle in marine stratocumulus. Part I: impact of drizzle on the formation and evolution of open cells. *Journal of the Atmospheric Sciences*, 66(11), 3237–3256. Available from: https://doi.org/10.1175/2009JAS3022.1

Wielicki, B., Barkstrom, B., Harrison, E., Lee, R., Smith, G. & Cooper, J. (1996) Clouds and the earth's radiant energy system (ceres): an earth observing system experiment. *Bulletin of the American Meteorological Society*, 77, 853–868. Available from: https://doi.org/10.1175/1520-0477(1996)077<0853:CATERE>2.0.CO;2

Wolding, B., Rydbeck, A., Dias, J., Ahmed, F., Gehne, M., Kiladis, G. et al. (2024) Atmosphere–ocean coupled energy budgets of tropical convective discharge–recharge cycles. *Journal of the Atmospheric Sciences*, 81(1), 3–29. Available from: https://doi.org/10.1175/JAS-D-23-0061.1

Wulfmeyer, V., Muppa, S.K., Behrendt, A., Hammann, E., Späth, F., Sorbjan, Z. et al. (2016) Determination of convective boundary layer entrainment fluxes, dissipation rates, and the molecular destruction of variances: theoretical description and a strategy for its confirmation with a novel lidar system synergy. *Journal of the Atmospheric Sciences*, 73(2), 667–692. Available from: https://doi.org/10.1175/JAS-D-14-0392.1

Yoneyama, K., Zhang, C. & Long, C.N. (2013) Tracking pulses of the madden–julian oscillation. *Bulletin of the American Meteorological Society*, 94(12), 1871–1891. Available from: https://doi.org/10.1175/BAMS-D-12-00157.1

Zuidema, P., Li, Z., Hill, R.J., Bariteau, L., Rilling, B., Fairall, C. et al. (2011) On trade wind cumulus cold pools. *Journal of the Atmospheric Sciences*, 69(1), 258–280. Available from: https://doi.org/10.1175/JAS-D-11-0143.1

SUPPORTING INFORMATION

Additional supporting information can be found online in the Supporting Information section at the end of this article.

> **How to cite this article:** Acquistapace, C., Schnitt, S., Krause, S., Risse, N., Lange, D. & Chatterjee, D. (2025) Characterizing trade-wind shallow convection regimes in the open sea with a synergy of ship-based vertical profiling observations. *Quarterly Journal of the Royal Meteorological Society*, e70038. Available from: https://doi.org/10.1002/qj.70038